

¹ Real-time spectral radiance estimation of hemispherical clear skies ² with machine learned regression models

³ Joseph Del Rocco^{a,*}, Paul D. Bourke^b, Charles B. Patterson^c and Joseph T. Kider^a

⁴ *^aIST, School of Modeling, Simulation, & Training, University of Central Florida, Orlando, FL, USA*

⁵ *^bUniversity of Western Australia, Crawley WA, Australia*

⁶ *^cFull Sail University, Winter Park, FL, USA*

⁷ ARTICLE INFO

¹¹ **Keywords:**

¹² sky radiance

¹³ spectral radiance

¹⁴ all sky

¹⁵ machine learning

¹⁶ building performance

¹⁷ HDR

¹⁸

¹⁹

²⁰

²¹

²²

²³

²⁴

ABSTRACT

Whole sky spectral radiance distribution measurements are difficult and expensive to obtain, yet important for real-time applications of radiative transfer, building performance, physically based rendering, and photovoltaic panel alignment. This work presents a validated machine learning approach to predicting spectral radiance distributions (350–1780 nm) across the entire hemispherical sky, using regression models trained on high dynamic range (HDR) imagery and spectroradiometer measurements. First, we present and evaluate measured, engineered, and computed machine learning features used to train regression models. Next, we perform experiments comparing regular and HDR imagery, sky sample color models, and spectral resolution. Finally, we present a tool that reconstructs a spectral radiance distribution for every single point of a hemispherical clear sky image given only a photograph of the sky and its capture timestamp. We recommend this tool for building performance and spectral rendering pipelines. The spectral radiance of 81 sample points per test sky is estimated to within 7.5% RMSD overall at 1 nm resolution. Spectral radiance distributions are validated against libRadtran and spectroradiometer measurements.

²⁵

²⁶ 1. Introduction

Atmospheric spectral radiance distributions, for ultraviolet (UV), infrared (IR) and visible spectra, for the entire sky, are often simplified into a single downwelling irradiance measurement, mainly because whole sky spectral radiance is difficult and expensive to measure in real-time and complicated to model. Yet precise radiance distributions are still very much needed for accurate calculations in real-time applications of building performance (Hensen and Lamberts, 2012; Chandrasekhar, 2013; Jakica, 2017), environmental science (López-Álvarez et al., 2008), photo-voltaic (PV) alignment (Smith et al., 2016), and physically based rendering (Jakob, 2010; Hosek and Wilkie, 2012; Satylmýs et al., 2016). Unlike irradiance, spectral radiance is directional and should be available for any point in the sky, as simulations are affected by the angle of incidence of spectral sky energy and receiving surface.

We present a data-driven machine learning approach to estimate spectral radiance for any point in a clear sky to within acceptable tolerances for real-time applications. We use high dynamic range (HDR) photographs of the sky and validated spectral radiance measurements captured throughout an entire year by a custom sky scanning framework (Kider et al., 2014), to train models that learn a relationship between capture time, sky appearance, and underlying energy (350–1780 nm). The primary contribution of our research is the reconstruction of high-dimensional atmospheric spectral radiance for every single point in a clear sky, including non-visible spectra (UV and near IR), given only a low-dimensional digital photograph of the sky and its capture time. We show that a clear sky photograph can be used to predict non-visible (and visible) atmospheric radiance energy.

Notable previous data-driven approaches to model skylight include Tohsing et al. (2014), Saito et al. (2016), and López-Álvarez et al. (2008); Cazorla et al. (2008a,b). Tohsing et. al leveraged ground-based sky radiance photographs and a non-linear regression model per wavelength to reconstruct only the visible spectrum. Saito et. al used total ozone column readings, camera color matching functions, and a linear algebra approach to predict a subset of visible for a single point in the sky. Cazorla et al. used neural networks, genetic algorithms, and regression models for specific points in the sky. Much of that work was performed on limited sets of data, and in some cases only a few hours of

*Corresponding author.

✉ jdelrocco@ist.ucf.edu (J. Del Rocco)

ORCID(s):

Nomenclature

$L_{e\Omega\lambda}$	spectral radiance distribution ($\text{W/m}^2/\text{nm}/\text{sr}$)
$(P\theta, P\phi)$	sky point of interest (azimuth, altitude) ($^\circ$)
$(S\theta, S\phi)$	sun location (azimuth, altitude) ($^\circ$)
(x, y)	sky image pixel coordinate
σ	standard deviation
SPA	sun point angle ($^\circ$)
ETR	extra trees regression model
RFR	random forest regression model
KNR	k-nearest-neighbor regression model
LNR	linear regression model
R^2	coefficient of determination score [-1, 1]
RMSD	root mean squared deviation (%)

49 single sky cover used for training (Tohsing et al., 2014). Our dataset is much more comprehensive. And our methods
 50 predict a wider, more useful spectral range, for every point in the sky. Furthermore, we show the reconstruction of
 51 non-visible energy from photometric inputs.

52 In this work, four separate regression models are developed through machine learning, with a combination of input
 53 features from correlated sky imagery and validated spectral radiance measurements. A series of new experiments are
 54 performed to test model effectiveness and efficiency with regards to changes in exposure, sky sample color model, and
 55 spectrum resolution. A tool is developed that uses a single model to predict spectral radiance distributions for every
 56 point of a hemispherical sky, at 1 nm resolution. Spectral radiance distributions are validated against libRadtran, a val-
 57 idated radiative transfer software package for atmospheric science (Emde et al., 2016; Buras and Mayer, 2011; Mayer
 58 and Kylling, 2005; Kylling et al., 1995; Dahlback and Stammes, 1991; Stammes et al., 1988).

59 We explain in Subsection 3.1 that this work focuses on clear skies by design. In our initial work (Del Rocco et al.,
 60 2018), we showed that regression models were not the best solution for scattered and overcast skies, despite the fact
 61 that one of the models showed promise. We believe a more complex machine-learning solution is needed to under-
 62 stand the more complicated patterns behind cloudy sky radiance. In contrast to more traditional atmospheric models,
 63 we purposely omit aerosol optical depth (AOD) and trace gas measurements to test viability of our methods today
 64 in real-time applications (commodity building monitoring systems, residential solar installations, rendering pipelines,
 65 etc.), which often do not have access to accurate sky measurements needed for complex physically-based solutions.
 66 Our proposed methods can accommodate readily available AOD and other atmospheric measurements as training and
 67 prediction features. Such features may even help our models adapt to localized turbidity.

68 The remainder of this paper is organized as follows. First, related work is presented in Section 2. Our measurements
 69 and engineered data is detailed in Section 3. We present our methods and experiments in Section 4, results in Section 5,
 70 and validations in Section 6. Finally, conclusions and future work are presented in Section 7.

71 2. Related work

72 Skylight itself has been studied for well over one hundred years (Strutt, 1871; Mie, 1908). Skylight simulation
 73 models typically fall into one of three categories. Early work often simplified solar and sky models by simulating lu-
 74 minance distributions and salient color characteristics with simple analytical equations. Later, the atmospheric science
 75 and computer graphics communities, separately and simultaneously, proposed brute-force physically-based simulations
 76 of light transport in the atmosphere using the radiative transfer equation (RTE) (Chandrasekhar, 1950; Mishchenko
 77 et al., 2002; Chandrasekhar, 2013). More recently, in the “big data” era, some researchers have attempted to model
 78 skylight with data-driven approaches, which often measure, process, and quantify large sets of data and search for cor-
 79 relations, usually with machine learning approaches. Modern atmospheric measuring systems installed at labs around
 80 the world are powerful and accurate, but often expensive and slow, and thus commodity sky scanning systems are more

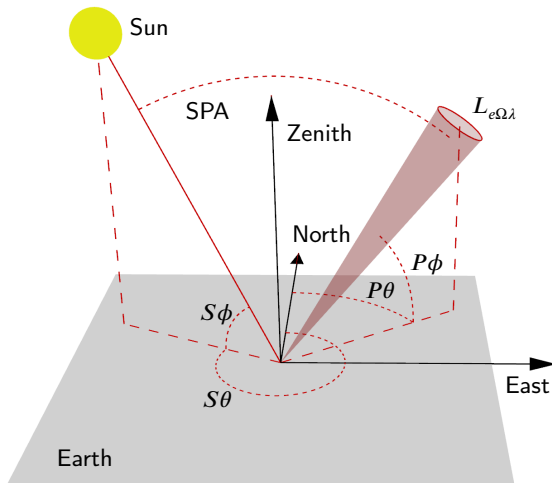


Figure 1: This figure explains the coordinate space and sky coordinates of measurements used in this work. A single atmospheric spectral radiance measurement ($L_{e\Omega\lambda}$) is measured at sky coordinates ($P\theta, P\phi$) (azimuth, altitude), taken from the ground by a custom sky scanning system. 81 such measurements were taken per sky capture. The sky coordinates of the sun ($S\theta, S\phi$) were computed with NREL's solar position algorithm. The central angle between sun location and sky point of interest is denoted as sun-point-angle (SPA) (Chauvin et al., 2015).

81 feasible for modern building performance solutions needed today (Butler, 2008; Mazria and Kershner, 2008).

82 2.1. Analytical methods

83 Analytical skylight models fit parametric functions to observations of the sky (Pokrowski, 1929; Kittler, 1994).
 84 Such models were standardized by The International Commission on Illumination (CIE) to calculate the spatial dis-
 85 tribution of skylight, and are based on measurements of luminance, indirect sky irradiance, and direct solar radiance.
 86 Early analytical approaches include the Intermediate Sky by Nakamura et al. (1985) and the UK Building Research
 87 Establishment (BRE) average sky by Littlefair (1981). Lee Jr (2008) studied overcast skies to find meridional consis-
 88 tencies. Cordero et al. (2013) studied albedo effect on radiance distributions (both upwelling and downwelling). One
 89 of the most popular analytical models is the all-weather model by Perez et al. (1993), which formulated a mathemat-
 90 ical equation with five coefficients to model sky luminance. This model was extended by Preetham et al. (1999) to
 91 calculate sky color values by fitting equations to a brute-force physically-based simulation. Hosek and Wilkie (2012)
 92 made several improvements including ground albedo, more realistic turbidity, and the handling of spectral compo-
 93 nents independently. Igawa and Nakamura (2001) and Yao et al. (2015) also improved the Perez all-sky model. All of
 94 these models produce realistic looking results, but often suffer from inaccuracies (Zotti et al., 2007; Kider et al., 2014;
 95 Bruneton, 2016).

96 2.2. Physically-based methods

97 Physically-based skylight methods produce the highest quality results of simulating skylight. They directly calcu-
 98 late the transfer of solar radiation in the atmosphere through the radiative transfer equation (RTE). They also directly
 99 calculate the composition of the atmosphere through Rayleigh and Mie scattering, and polarization. The atmospheric
 100 research community developed programs such as 6SV (Vermote et al., 2006), SMARTS2 (Gueymard et al., 1995),
 101 MODTRAN (Berk et al., 2014), and SBDART (Ricchiazzi et al., 1998), which produce accurate results, but often at
 102 high computational cost unsuitable for real-time applications. They also tend to focus on luminance and irradiance.
 103 libRadtran (Emde et al., 2016; Mayer and Kylling, 2005) is a popular, validated software package with various RTE
 104 solvers for atmospheric spectral radiance, irradiance, and other solar and sky properties, and is highly configurable. We
 105 use it to validate our model predictions. Like all physically-based solutions, libRadtran requires aerosol and particulate
 106 parameters and distributions (Hess et al., 1998; Holben et al., 1998) describing the sky, to produce the most accu-
 107 rate simulations. An alternative physically-based approach involves even more intricate, though perhaps even more
 108 accurate, multi-scattering calculations to reconstruct spectral radiance across varying sky covers (Kocifaj, 2015, 2012,

109 2009). These calculations require accurate atmospheric measurements. Separately, the computer graphics community
 110 also has developed numerous Monte Carlo based approaches (Nishita et al., 1993, 1996; Haber et al., 2005; Jarosz,
 111 2008) that merge the RTE with the rendering equation (Kajiya, 1986). These methods produce pleasing visual results
 112 and often approximate the complicated scattering calculations with phase substitutions by Henyey and Greenstein
 113 (1941) or Cornette and Shanks (1992).

114 2.3. Data-driven methods

115 In an increasingly “big data” era, where storage is cheap and data volume, velocity, and variety continues to increase
 116 exponentially, many scientists have taken a data-driven approach to solving problems (Gandomi and Haider, 2015;
 117 Sagiroglu and Sinanc, 2013; Chen et al., 2012; Laney, 2001). For modeling skylight, scientists systematically gather
 118 measurements and apply search algorithms to help model and simulate. This includes the capturing of high dynamic
 119 range (HDR) imagery (Stumpfel et al., 2004), image-based lighting, and irradiance and radiance measurements, to
 120 estimate luminance values for the sky directly from captured photographs.

121 The most relevant work to our own comes from Tohsing et al. (2014), the most comprehensive data-driven approach
 122 to date, who used 1143 separate machine learned regression models (one per color component (RGB) per wavelength
 123 of the visible spectrum (380-760 nm)) to estimate whole sky radiance. The authors trained and tested clear and cloudy
 124 skies separately and the entire dataset was captured over a period of 12 days. 113 samples from a 3.5 hour window of a
 125 single clear sky day were used for training. Whole sky scans took 12 minutes to complete, and thus a synthetic image
 126 was used for color sampling. Our data capture was much more comprehensive, spanning an entire year, accounting
 127 for seasonal variation. Skies were captured under 3 minutes, avoiding synthetic imagery (Del Rocco et al., 2018). Our
 128 methods predicts a much wider spectrum of energy (350-1780 nm), including some UV and IR, which is useful for
 129 a variety of applications. We also provide predictions for every single point in a hemispherical sky image. Finally, as
 130 opposed to a system of 1143 regression models, a single regression model is used to predict.

131 Saito et al. (2016) improved upon the work of Sigernes et al. (2008) to estimate sky radiance, specifically “*without*
 132 *any training sets*,” by using an equation of total ozone column and raw sky image red-green-blue (RGB) counts. They
 133 focused on the zenith of the sky (single point) and estimated spectral radiance for a subset of visible wavelengths (430-
 134 680 nm). They too treat clear and cloudy skies separately. A notable contribution is the color matching functions,
 135 which took into account camera lens wavelength dependence, vignetting, and CMOS noise, and were used for cloud
 136 detection in Saito and Iwabuchi (2016). This method should be scaled to include every single point of a sky image,
 137 both clear and cloudy, and validated against a radiative transfer package.

138 Artificial neural networks (ANN), genetic algorithms, and pseudoinverse linear regression models were used in
 139 various projects by López-Álvarez et al. (2008); Cazorla et al. (2008a,b). They also used a custom sky scanner. Their
 140 models focused on visible spectra with a final dataset of 40 samples. More recently, Satylmýs et al. (2016) used an
 141 ANN to model certain properties of skylight.

142 Chauvin et al. (2015) used a custom sky imaging framework for irradiance and cloud detection for the purposes of
 143 concentrating solar plant technology. A noted contribution was their observation of the importance of the circumsolar
 144 region, in opposition of many sky models, and the central angle between sun position and sky point of interest, or
 145 sun-point-angle (SPA). Their research was used for intrahour forecasting to improve solar resource acquisition (Nou
 146 et al., 2018).

147 Our research: (1) reconstructs the spectral radiance of the sky utilizing high resolution imagery, (2) accounts for
 148 seasonal and datetime variation with captures throughout an entire year, (3) accounts for fisheye lens warp, (4) predicts
 149 a wide, useful spectrum of energy (350-1780 nm) at 1 nm resolution, (5) predicts non-visible spectrum energy with
 150 indirect visible data (a novelty), (6) does so for an entire hemispherical clear sky image, (7) tests multiple exposure im-
 151 agery, color model, and spectral resolution, (8) considers real-time constrained downstream applications of this work,
 152 (9) trains and compares multiple regression models, and (10) validates spectral radiance predictions against a modern
 153 atmospheric radiative transfer software package.

154 3. Measurements and data

155 Measurements in this work come from the sky scanner discussed in detail by Kider et al. (2014). This framework
 156 captured high-resolution HDR imagery of the sky (8 exposures), along with atmospheric spectral radiance distributions
 157 (350-2500 nm) from 81 sample points in concentric circle patterns across the sky. Measurements were taken from the
 158 ground. The sampling pattern is arbitrary, but was designed to capture a uniformly distributed “skeleton” of measure-

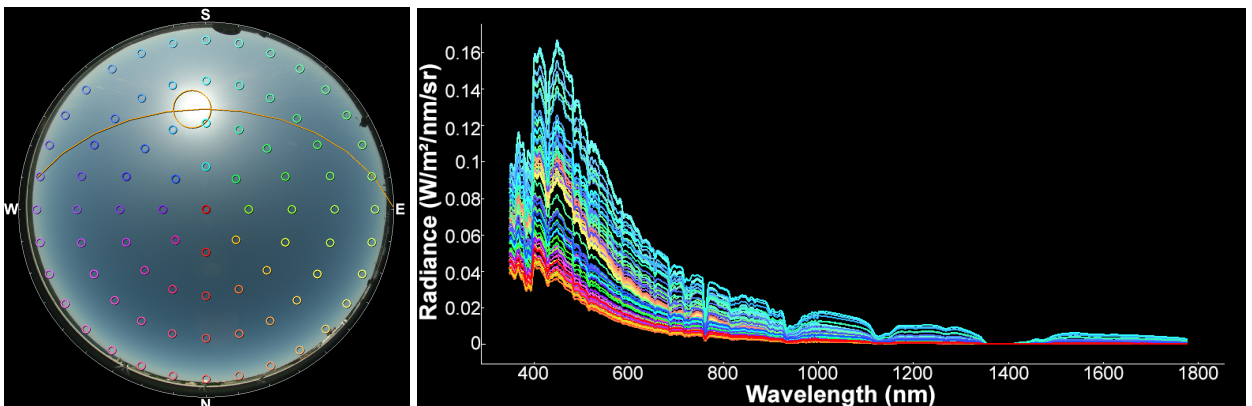


Figure 2: A single sky capture consisted of high-resolution imagery and 81 spectral radiance measurements between 350-2500 nm (350-1780 nm used for this work). (a) shows the sky coordinate locations of the 81 radiance measurements projected onto a sky image; in other words, where in the sky each measurement was made. The sun's location and path is depicted in orange. (b) shows the correlating radiance measurement values in $\text{W} / \text{m}^2 / \text{nm} / \text{sr}$ between 350-1780 nm. The colors of each sky location in (a) correlate with radiance distributions in (b). As expected, radiance measurements taken closer to the sun are higher. The radius of colored circles is not to exact scale with sampled pixel area used in methods described in this work.

ments across the sky. The spectral radiance distributions were measured in $\text{W} / \text{m}^2 / \text{nm} / \text{sr}$ with an ASD FieldSpec Pro spectroradiometer through a 1° solid angle fore-optic (Malthus and MacLellan, 2010), and were validated against NASA datasets (Kider et al., 2014). The multiple exposure photographs of the sky were captured in both CR2 (raw) and JPG formats consecutively at 4368 x 2912 pixels with a commodity Canon 5D digital single-lens reflex (DSLR) full-frame camera with underlying complementary metal-oxide-semiconductor (CMOS) image sensor, together with a Sigma 8 mm f/3.5 EX DG circular fisheye lens, and a Kodak Wratten neutral density filter. JPG compression quality level was set to 100. We automated the process with libgphoto2, which took approximately 40 s to capture all exposures and formats of photographs of the sky. Irradiance was also measured, but ignored for the purposes of this work.

All measurements were taken at a single site location, (42.44344, -76.48163) decimal degrees, on the rooftop of Frank Rhodes Hall, Cornell University, Ithaca, New York, USA. 453 total sky captures were taken over 16 days between 2012-2013, covering all four seasons, dawn to dusk, and various sky covers, for a total of over 36000 individual spectral radiance measurements. Roughly 25% of the captures consisted of full clear skies (0 octas of clouds), from which 6006 individual clear sky samples were used for this work. Scattered and overcast skies were purposely left out of this work to focus our efforts. A complete table listing of all usable data that we captured can be found in Del Rocco et al. (2018). This dataset is freely available to the public through the project website.¹

Hemispherical sky coordinates are specified in (azimuth, altitude) coordinates, where azimuth is an angle Eastward from North, and altitude is (90° – zenith). Sky imagery is vertically flipped due to capture orientation. The correlation of validated radiance measurements and sky color at the same sky coordinates is explained in Subsection 3.2 and Subsection 3.3.

3.1. Sky cover

As mentioned, our entire dataset includes a variety of sky cover conditions, roughly 25% clear skies, 67% scattered, and 8% completely overcast. We assessed sky cover manually with our dataset browsing tool, even though procedural assessment is possible. We used the categorization of sky conditions provided by the US National Oceanic and Atmospheric Administration (NOAA) (Office Of The Federal Coordinator For Meteorological Services And Supporting Research, 2017), designating skies as clear (CLR), scattered (SCT), and overcast (OVC). CLR and OVC skies contained 0 and 8 oktas of cloud cover, respectively. We used SCT for any sky with cloud coverage between 1-7 oktas. The distinction of few (FEW) and broken (BKN) skies was ignored to minimize the number of machine learning models necessary for downstream applications.

As discussed in our preliminary work (Del Rocco et al., 2018), we initially trained and tested sky samples of all

¹ <https://github.com/spectralskylight>

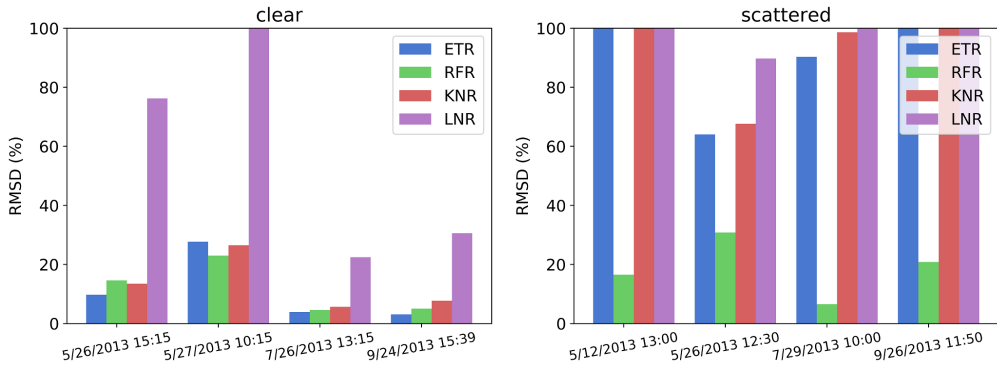


Figure 3: Preliminary results on sky cover specific datasets from Del Rocco et al. (2018). In general, our proposed method performs better on clear skies. One of our models showed promise on scattered cloudy skies, but we focus on clear skies for this work.

sky covers. We then found that our regression models performed dramatically better when tested on sky cover specific datasets. Although we were able to show that at least one regression model performed admirably well on scattered skies, we surmised for the time being that perhaps more complicated models (e.g. deep learning neural networks) were best suited to model the likely non-linear relationships of scattered and overcast skies and spectral radiation. Therefore the work proposed here is our most refined approach of using regression models on clear skies specifically. This includes validation of our predictions with a validated radiative transfer software package, more experiments, spectral radiance predictions for every single pixel of a sky photo, the use of multiple exposures (HDR), the accommodation of lens linearity, sky samples within the circumsolar region, and more accurate whole sky error plots.

As the title of this work suggests, the regression model approach presented is currently not unified across all sky covers. The process of separating clear, scattered, and overcast skies has been discussed in many prior papers, using metrics such as clear-sky index, R/B ratio, fractional cloud cover, colormetric and spectral combined metric, etc. (Arking and Childs, 1985; López-Álvarez et al., 2008; Cazorla et al., 2008b; Yamashita et al., 2004; Li et al., 2011; Saito and Iwabuchi, 2016; Nou et al., 2018). There are two valid procedural approaches to using our models. Either categorize the entire sky into buckets of CLR, FEW, BKN, SCT, OVC (or any other distinction), and use a capture of the sky with an appropriate model, or separate clear from cloudy samples from parts of each sky and pass samples to separate models for prediction.

3.2. Lens linearity

Because our work involved mapping hemispherical sky coordinates to 2D pixel coordinates, and vice versa, it was important to accurately model the behavior of the fisheye lens employed. In a perfect circular fisheye lens, often called a "tru-theta" lens, equal increments in radius on the fisheye image correspond to equal angle increments of the respective field rays. Actual fisheye lenses typically exhibit some form of non-linearity, even those lenses designed to be linear (Bourke, 2016). Although more important with variegated skies (scattered, overcast, etc.), a measurement difference of even a single degree can result in sampling pixels in or out of the sun's corona. The standard ideal lens equation for mapping hemispherical sky coordinates to 2D center offset coordinates can be written as:

$$(x, y) = \frac{2 \cdot \text{zenith}}{\text{fisheyefov}} \cdot (\cos(\text{azimuth}), \sin(\text{azimuth})). \quad (1)$$

The following procedure was used to measure the relationship between field angle and position on the image:

1. A close and distant vertical feature in the fisheye image was chosen. The zero parallax position of the lens is the position along the lens axis where those features stay aligned despite rotations perpendicular to the lens axis.
2. A clear narrow object in the image was chosen as a reference point and aligned with the center of fisheye image.
3. The lens is rotated in 5° steps from 0 to 90°, and a photograph taken.
4. For each photograph, the distance of the reference point from the center was measured.

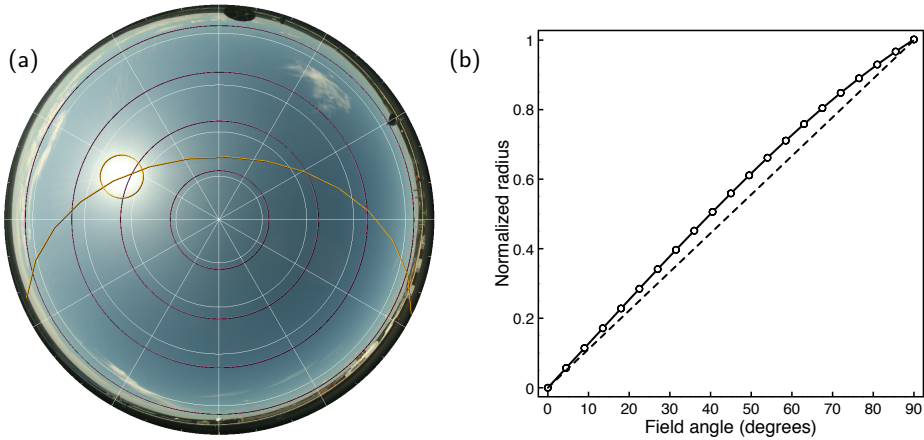


Figure 4: This figure visualizes the linearity of our lens, or the differences ("lens warp") between an ideal fisheye lens and the lens we used in this work. (a) plots the altitudes 12.1151° , 33.749° , 53.3665° , and 71.9187° (altitudes of radiance measurements) for our actual lens (magenta) vs an ideal fisheye lens (white). The deviation, in terms of number of pixels, is not insignificant. The computed location and path of the sun, after lens correction, is overlaid (orange). (b) plots sample points from a lens linearity calibration experiment from our actual lens (solid line) vs an ideal fisheye lens (dashed line). The sample points of the solid line were used to fit Eq. 2.

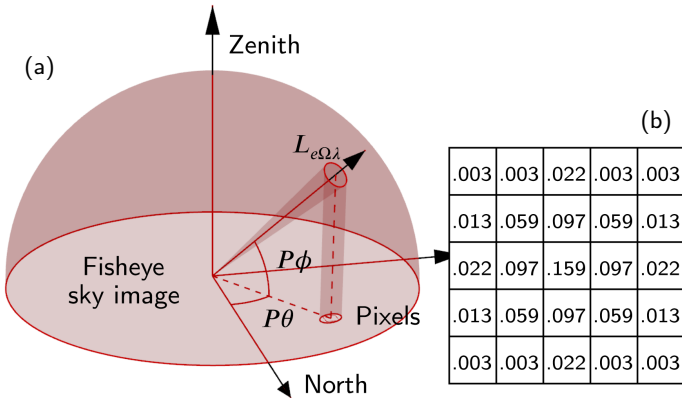


Figure 5: Here we show the standard radiometry of measuring the steridian area of a single sky sample, one of 81 spectral radiance measurements at sky coordinate $(P\theta, P\phi)$ (azimuth, altitude), whose coordinate is then projected onto a 2D photo of the sky. (a) shows the captured steridian area projected onto the sky image, the bounds of which contain the pixels of interest for that sky sample; (b) shows the weights of a 5×5 Gaussian convolution matrix which is applied to the pixels in those bounds to compute a final color for that sky sample.

218 For our Sigma 8 mm f/3.5 fisheye lens, this resulted in the following non-linear curve (plotted in Fig. 4), which was
219 then used to alter zenith of sky coordinates ($r = \text{zenith}$):

$$r' = 0.7230r + 0.0252r^2 - 0.0499r^3 - 0.0004325r^4. \quad (2)$$

220 3.3. Sky color sampling

221 Color at a particular location in the sky is a fairly subjective measure. What our eyes detect, what instruments
222 measure, and how that data is processed, differs dramatically. Nevertheless, our research investigates the relationship
223 between sky color and energy distribution, and thus a quantitative metric must be used.

224 To quantify sky color at specific points in the sky, we projected the bounds of a 1° solid angle (same as fore-optic
225 we used when measuring radiance) onto the 2D sky images captured with our digital camera (multiple images for the

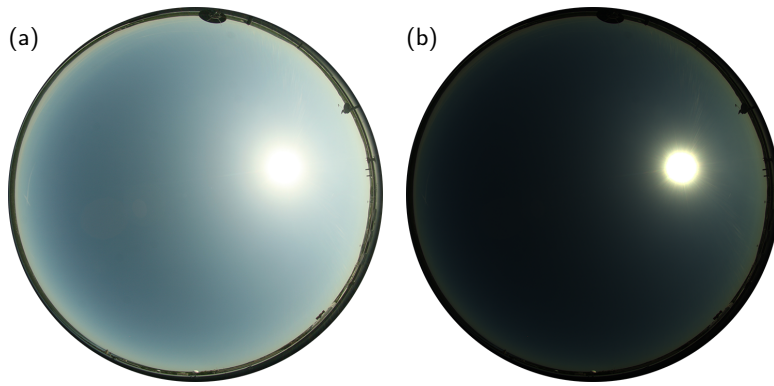


Figure 6: 05/27/2013 09:00 1s exposure of sky as a more traditional, camera processed, compressed JPG (a), and as a minimally processed, uncompressed TIFF (b). (a) approximates what humans see when looking at the sky, but (b) is more accurate in terms of what the DSLR CMOS sensor measures.

226 HDR experiment), and then sampled the pixel colors with a square convolution of similar width to the radius (Fig. 5).
 227 In other words, when exporting data associated with a sky capture, we correlate the 81 radiance measurements with
 228 81 pixel samplings of a sky photo, at the same lens linearity corrected coordinates projected to 2D.

229 More than a single pixel was used to estimate sky color at each sampled sky location because the corresponding
 230 spectral radiance measurement was captured within a 1° steridian. To estimate the equivalent color, we used a common
 231 image processing technique known as convolution, which involves sliding a matrix of weights or homogeneous values
 232 (the kernel) over a set of image pixels in order to compute a new set of pixels (Parker, 2010). Such convolutions are
 233 used to implement a wide variety of image filters like blurring, edge highlighting, etc. We used a Gaussian convolution,
 234 in particular, to blend the pixel colors together, weighting pixels closer to the center higher than pixels near the edges
 235 of the projected bounds.

236 We note that a square convolution does not account for all pixels in a projected circular area exactly; in fact, the
 237 projected circle becomes an increasingly oblong ellipse as altitude decreases. A rectangular convolution kernel would
 238 likely provide better coverage of the pixels in the projected bounds. Our kernel was chosen for real-time efficiency and
 239 overlap with existing image processing techniques and libraries, most of which use square kernels. The weights of our
 240 Gaussian kernels were generated with the following equation (Fisher et al., 1996):

$$\text{kernel}(x, y) = \frac{1}{2\pi\sigma^2} \cdot e^{-\frac{x^2+y^2}{2\sigma^2}}, \quad (3)$$

241 with kernel dimensions relative to the bounds of the convolution, and a standard deviation (σ) of half the radius.

242 3.4. Raw vs. digital positive

243 As mentioned, we captured photographs in a Canon CR2 (raw) format and a more traditional, camera processed,
 244 compressed JPG file format. Raw images contain much more capture information in a pre-interpolated format, before
 245 debayering, noise filtering, color space conversions, gamma correction, etc. In our previous work, we worked with the
 246 compressed JPG captures, which were smaller and faster to process (Del Rocco et al., 2018). For this work, we strove
 247 for accuracy of recorded color values and interpolated the raw photographs into uncompressed TIFF files, using camera
 248 white balance, but no other post-processing options that digital cameras use to produce images closer to what humans
 249 see (e.g. gamma correction, additive brightness, exposure shift, etc.). We used rawpy to read and process the raw
 250 images (Riechert, 2018; LibRaw). Fig. 6 shows the difference. Our previous work already showed that it is possible to
 251 infer a relationship between sky appearance and spectral radiance using compressed imagery. The consistency of raw
 252 photograph interpolation may be more crucial than the specific parameters used.

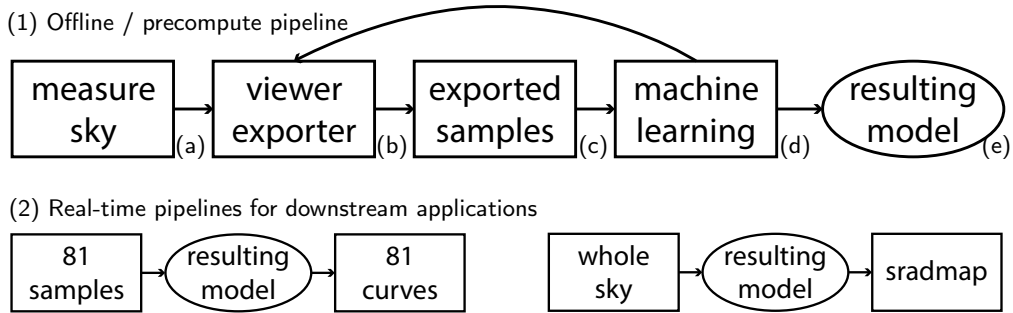


Figure 7: Our method is split into two parts, (1) offline learning to produce a model for (2) real-time application use. (a) is described in Kider et al. (2014). (b) is our viewer/exporter tool used to correlate, inspect, and export datasets. (c) is the clear sky dataset used for this work; each sample of which contains the features depicted in Fig. 8. (d) consists of the methods described in Section 4. While testing on the non-holdout portion of our dataset, identifying data anomalies, incorporating lens linearity equations and adding engineered features, resulted in data being reexported. (e) represents one of our four final regression models produced from this work. In (2), the input features of 81 sky samples from each of our four holdout test skies (Table 1) are passed through a model to predict spectral radiance distribution, which are compared to their corresponding ground truth measurements to produce error plots and validated against libRadtran. Finally, a whole sky image can be passed through a model to produce a spectral radiance map (sradiomap), where each “pixel” is a spectral radiance distribution.

253 4. Methods and experiments

254 The research question for this work asks whether it is possible (or not) to estimate the atmospheric radiance distribution
 255 of a clear sky given only a picture of said sky and its capture timestamp. In other words, is there a relationship
 256 between what a commodity camera sees in the sky, the time of day, and the underlying spectral energy, despite the
 257 fact that we know solar radiation scattering is a complex process where energy is absorbed and scattered by atmo-
 258 spheric particles at certain wavelengths? Is it possible for mere photos of the sky to give acceptable/useful estimates
 259 of energy for use in downstream applications? In this work, we propose a data-driven method (machine learning on a
 260 dataset of measurements) to help us search for such a relationship. But given the sheer magnitude of machine learning
 261 approaches (statistical models, artificial neural networks, support vector machines, etc.), we limit the scope of this
 262 research to regression models. Predicting a curve (i.e. not a single output) is more of a regression problem, as opposed
 263 to classification or clustering.

264 A supervised approach is natural, given our measurements and problem formulation. Given photos of skies, their
 265 capture timestamp, and 81 corresponding spectral radiance measurements (curves/distributions) per sky, is there a cor-
 266 relation? The radiance measurements are natural ground truths for what a camera sees at those 81 points in the sky. As
 267 mentioned, we focused on clear sky measurements, specifically 6006 samples (or ~17% of our entire data set), where
 268 each sample represented a single point in a clear sky coupled with capture timestamp and corresponding spectral ra-
 269 diance measurement. In our initial approach (Del Rocco et al., 2018), we culled all samples within a 20° circumsolar
 270 region, like prior authors Saito et al. (2016) and Tohsing et al. (2014). The work of Chauvin et al. (2015), who investi-
 271 gated the radiance profile within the circumsolar region, encouraged us to use all valid sky samples. Samples closer
 272 to the sun are important, as the bulk of energy comes from this area of the sky.

273 We developed a viewer / exporter / converter tool to manage our large dataset and export subset collections of data
 274 (Del Rocco et al., 2018) and (Fig. 7(1b)). Our collection of exported clear sky samples was then partitioned into an
 275 80:20 train/test:holdout ratio, where samples from four arbitrary skies (Table 1), selected at random, were kept in the
 276 holdout partition. The train/test partition was then randomized with the same pseudorandom seed to keep the training
 277 and testing data consistent across runs, and 10-fold cross-validation was utilized to allow us to divide this partition into
 278 training and testing separately while tuning the models. It was also used to dampen the effects of outliers on subsets of
 279 data (Picard and Cook, 1984; Kohavi et al., 1995). At no point in the tuning of models was the holdout data used for
 280 testing. These techniques are often employed to help minimize overfitting and data leakage.

281 Each sky sample of Fig. 7(1c) consisted of a vector of input and output features. From the raw measurements of
 282 capture timestamp, sample azimuth and altitude, sky color, and spectral radiance measurement, we engineered and

Table 1

Four holdout test skies selected at random. Table of all measurements listed in Del Rocco et al. (2018)

Date	Time	Part of Day	Season	Sky Cover
05/26/2013	15:15	Afternoon	Spring	CLR
05/27/2013	10:15	Morning	Spring	CLR
07/26/2013	13:15	Midday	Summer	CLR
09/24/2013	15:39	Afternoon	Fall	CLR

283 computed the additional features: sun azimuth and altitude, sun-point-angle (SPA), quarter, month, week, day and
 284 hour. The capture timestamp was initially included as a single integral feature, but was later “binned” (Macskassy and
 285 Hirsh, 2003) into discrete datetime groupings to help the models better account for seasonal and diurnal variation in
 286 clear sky turbidity (Elbaakh et al., 2012). Sun position was computed with the solar position algorithm provided by
 287 the US National Renewable Energy Laboratory (NREL) (Reda and Andreas, 2004). SPA comes from the insights of
 288 Chauvin et al. (2015), and was not included in our initial work.

289 Various exploratory data analysis (EDA) techniques (Fig. 9) were employed to gauge the significance of each
 290 possible input feature, including: histograms, correlation matrix, collinearity matrix, outlier detection, and feature
 291 importance (Yu, 1977). EDA scores are univariate and calculated by scikit-learn directly (Pedregosa et al., 2011). For
 292 correlation and collinearity, in general, the more correlated input features are to the output, the better they will perform
 293 as predictors, but the more correlated they are to each, the more overlap. F-measure (f-score) is the ratio of harmonic
 294 mean precision and recall, often used as a prediction effectiveness measure, is well documented in statistics literature,
 295 and included in most machine learning libraries (Cooper, 1973; Van Rijsbergen, 1979; Chinchor, 1992; Sasaki, 2007;
 296 Pedregosa et al., 2011).

297 As Fig. 9 shows, all datetime features are naturally correlated, but equally important. By binning the datetime, we
 298 hope the model captures seasonal and time of day variation, which has been shown to affect turbidity ((Elbaakh et al.,
 299 2012)). The three components of a single color sample (a Gaussian convolution of pixels within a 1° portion of the
 300 sky) are also naturally highly correlated. The hour of day feature likely correlates to sun azimuth more than altitude
 301 because on a 2D projected fisheye photo of the sky, the sun’s azimuth varies more than its altitude. Sky sample color
 302 components were found to be the most important features. When HDR data was investigated, longer (brighter) expo-
 303 sure were found to be more significant than shorter (darker) exposures. Initially, sample azimuth and altitude were of
 304 some importance, but after SPA was added, both sample azimuth and altitude scored as much less important, likely
 305 because SPA is a combination of both sun and sample locations in a single feature. The sample altitude feature was
 306 dropped completely. Sample azimuth was retained because tests without it affected results slightly (~2% RMSD). As
 307 Fig. 9(c) shows, 81 samples per capture evenly distributed across the sky resulted in a nearly flat distribution of sample
 308 azimuth values. The final input and output features of each sky sample used by our models are shown in Fig. 8.

309 More than 10 separate regression models were trained and tested, including: linear, Ridge (Hoerl and Kennard,
 310 1970), Lasso (Tibshirani, 1996), ElasticNet (Zou and Hastie, 2005), Lars, KNN, RandomForest (Kocev et al., 2013),
 311 ExtraTrees (Geurts et al., 2006), etc. Initially, WEKA toolkit (Hall et al., 2009) was used to discover possible candi-
 312 date models, but ultimately all machine learning models were configured and processed with scikit-learn in Python
 313 (Pedregosa et al., 2011). Initial tests of these models encouraged us to pursue the ones with promise. Many of the
 314 models forced a single decimal output value (not a vector), which didn’t align with our approach; we are attempting to
 315 reconstruct a curve, or vector of radiance values per wavelength. We chose a proximity based model, like k-nearest-
 316 neighbors (KNN), and a decision tree based (ensemble) model to focus on. We also included a standard linear regressor
 317 (LNR) as a baseline, which we assumed would not perform well given the nature of the data and problem. Decision
 318 tree models implement a set of “if-then-else” rules internally for both training and prediction, and result in very large
 319 model files. We know that decision tree estimators are more prone to overfitting than any other regression model, so
 320 to further address overfitting, we used a Random Forest Regressor (RFR) specifically, which harnesses randomness
 321 to decrease variance in lieu of some bias (Kocev et al., 2013). Extra Trees Regressor (Geurts et al., 2006) introduces
 322 even more randomness and a larger trade off to combat overfitting. The final collection of tuned regression models
 323 include a linear regression (LNR), k-nearest-neighbors (KNR), random forest (RFR), and extra-trees (ETR). Although
 324 the performance of RFR and ETR are often comparable, in prior experiments we found that RFR performed signifi-
 325 cantly better on scattered cloudy skies (Del Rocco et al., 2018). For all four of our models, tuning was done mostly

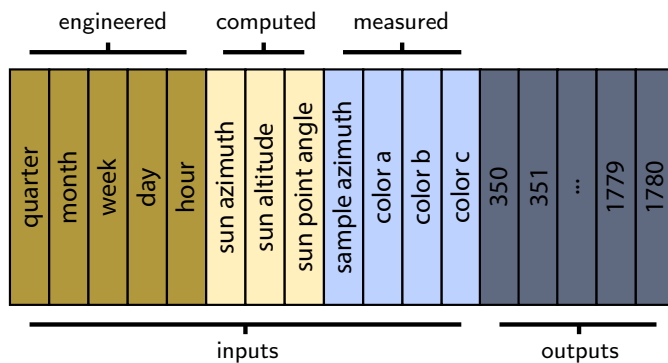


Figure 8: A single sky sample consists of 12 input features and 1430 output features (the spectral radiance curve between 350-1780 nm). Capture timestamp was binned into separate features to help capture seasonal variation. Sun azimuth and altitude were computed via NREL sun position algorithm. Sample azimuth and altitude were inherent to sky scanning logic, yet EDA found them to be of little importance. The three color features are components of single sky color per sample, relative to color model used (e.g. RGB, HSV, etc.).

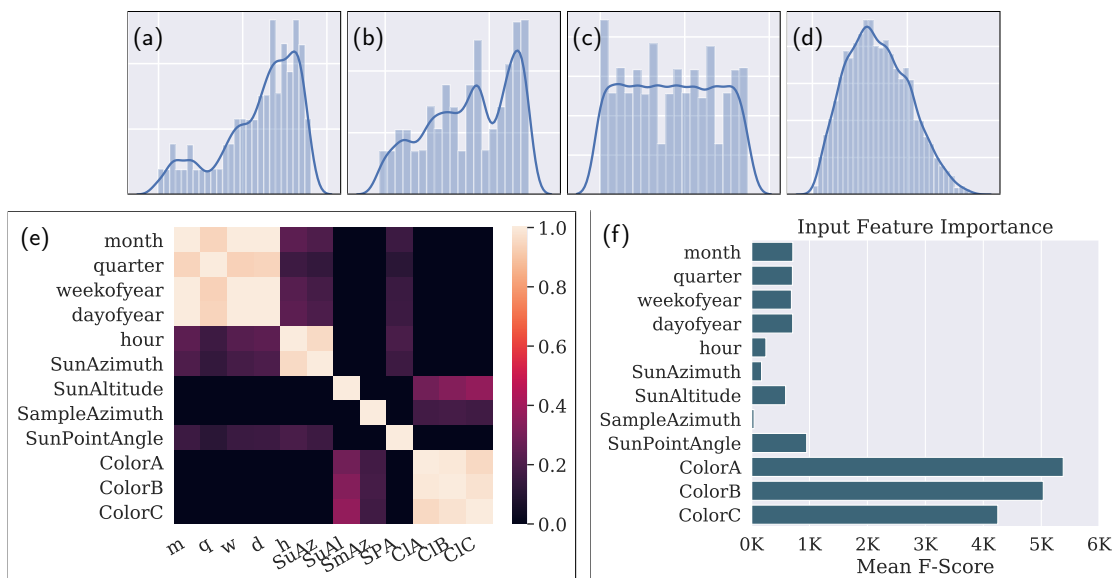


Figure 9: Plots of individual machine learning features, including histograms for (a) sun azimuth, (b) sun altitude, (c) sample azimuth, and (d) SPA. (e) shows the univariate correlation matrix of the features. Datetime components, color components, and hour of day with sun azimuth are all naturally correlated. (f) shows an estimation of importance (significance to prediction) of each feature. (d) was likely more significant because it combined the positions of both sun and sample points into a single feature. After SPA was included, sample altitude was discarded.

automatically with scikit-learn's GridSearch algorithm, though some hyperparameters were tuned manually, including the number of trees and maximum tree depth of the decision tree models.

Four separate error metrics were used to evaluate the performance of models, including: coefficient of determination score (R^2), mean bias deviation (MBD), root mean squared deviation (RMSD), and ratio of the measured and predicted radiance curves. MBD and RMSD come from Iqbal (2012):

$$RMSD = \sqrt{\frac{\sum_{i=1}^N (y_i - x_i)^2}{N}} \quad (4)$$

331 where N is the number of spectral radiance distributions considered, y the predicted distributions, and x the measured
 332 ground truth distributions. Recall that each distribution is a vector of radiance values between 350-1780 nm of the
 333 electromagnetic spectrum. Prior authors used MBD for single wavelength results (Cazorla et al., 2008a; Tohsing et al.,
 334 2014), but we found RMSD to be more representative of the results across a spectrum of wavelengths. The R^2 metric
 335 is used during pre-holdout testing to help with model tuning, and is calculated directly from scikit-learn:

$$R^2(t, p) = 1 - \frac{\sum_{i=1}^N (t_i - p_i)^2}{\sum_{i=1}^N (t_i - \bar{t}_i)^2}, \quad (5)$$

336 where (t, p) is a (truth, prediction) pair, N is the number of radiance distributions, and $\bar{t} = \frac{1}{N} \sum_{i=1}^N t_i$. Note that this
 337 metric can be negative, despite the name R^2 .

338 In addition to our dataset tool, we developed a framework of Python scripts to send datasets through our machine
 339 learning pipeline of training, final testing, and plotting. The main script takes parameters such as: model type, dataset
 340 of sky samples, pseudo-random number seed, number of cpu cores to use, cross-validation amount, and model-specific
 341 hyperparameters such as polynomial expansion amount, maximum tree depth for decision tree pruning, etc. All source
 342 code for dataset tool and pipeline is 100% cross-platform, open-source and freely available to the public through the
 343 project website.²

344 4.1. High-dynamic range imagery

345 Simultaneously capturing the sun and sky with photography is difficult due to the range of illumination and intensity
 346 of the sun vs. sky, as well as the temporal changes that occur. We followed the sky capture approach of Stumpfel et al.
 347 (2004). We took eight to nine photographs (depending on the time of day) to capture \sim 17 stops of dynamic range.
 348 Fig. 10 shows the difference in exposures captured; the top row (f/16 aperture) is best for the solar region and intensity
 349 of the sun; the bottom row (f/4 aperture) is best for the indirect skylight.

350 This experiment was designed to test the effectiveness of using HDR imagery (multiple exposures) vs. a single
 351 exposure of the sky. For each sky sample, we used the pixel color values from exposures 5-8 (f/4 aperture) as input
 352 features for model training and prediction. Exposures 1-4 were ignored for this experiment. Although there are algo-
 353 rithms to merge multiple exposures into a single image for sampling, we simply sampled each exposure separately and
 354 used each sampled color as a separate input feature. Future work could include a merged color feature.

355 4.2. Color model

356 Colors are qualia for combinations of electromagnetic energy within the range of wavelengths visible to humans
 357 (the visible spectrum). The human eye detects energy with the use of retinal rods and cones and the brain merges the
 358 results into what we call a color (Kinney, 1958). Modeling the values of these colors is a field of research in and of

² <https://github.com/spectralskylight>

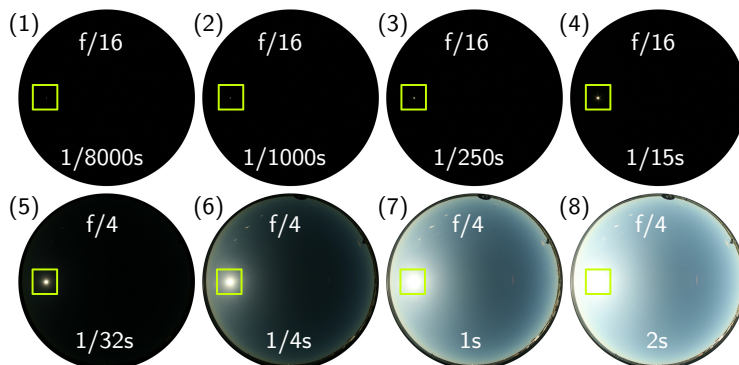


Figure 10: 8 exposures were taken to account for high dynamic range of sun + sky photography. f/4 aperture captures (5-8) were used for this work. 1 s exposure (7) was used for non-HDR experiments. Yellow squares highlight sun location.

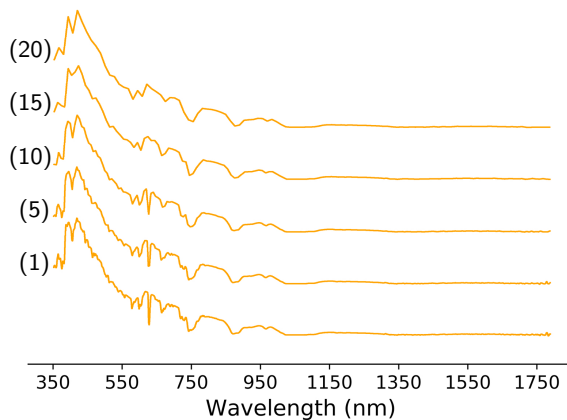


Figure 11: 05/26/2013 15:15 sample 24 (90° azimuth, 12.12° altitude) plotted at 5 different resolutions, 1, 5, 10, 15 and 20 nm, labeled accordingly. The resolution of spectral radiance distributions can be reduced depending on the downstream application.

359 itself (Koenderink, 2010). And yet, we are attempting to estimate spectral radiance using color values as a primary
 360 feature. This begs the research question: which color model best represents the underlying energy? Digital all-sky
 361 cameras typically store measurements with trichromatic RGB color models (e.g. sRGB, Adobe RGB, ProPhotoRGB,
 362 etc.), but do so mostly for historical reasons relating to technology. There are a variety of other tristimulus color models
 363 that attempt to capture more of the color space detectable by the average human (Poynton, 1995; Stone, 2015), many of
 364 which derive from the CIE 1931 RGB and XYZ color space definitions (Wright, 1929). However, it is unclear which
 365 model is most beneficial for machine learning algorithms processing sky images.

366 For this experiment, we compared the overall training and predictive effectiveness of our models while only chang-
 367 ing the color model used for each sky sample's color feature. Four separate color models were tested: sRGB (Stokes
 368 et al., 1996) (the default), HSV (Smith, 1978), HSL (Joblove and Greenberg, 1978), and LAB (Robertson et al., 1977).
 369 All other features were fixed. Because our commercial digital camera captured skies in an sRGB format, we then con-
 370 verted to the other color models using algorithms provided by the Python colormath module. The resulting datasets
 371 were fed through our machine learning pipeline separately.

372 4.3. Spectral resolution

373 This work is intended to be used in a real-time setting, both simulated and cyber-physical, therefore model size
 374 and processing speed is important. For applications that predict a general quantity of energy in certain parts of the
 375 spectrum, it may be reasonable to limit the resolution of spectral data used during model training and prediction.
 376 Certainly, the visual difference and area under the curve (amount of energy) between a 1 nm and 10 nm resolution
 377 curve is not significant. A spectral resolution experiment was designed to find the smallest model and dataset that
 378 still predicted with acceptable accuracy, by training and testing models using spectral resolutions of 1, 5, 10, 15 and
 379 20 nm. Note that some pure spectral colors exist entirely within a 15 nm range, and therefore resolution should not
 380 be diminished too much if color information is important. Fig. 11 shows the visual difference of the five resolutions
 381 for a single measured radiance distribution. Depending on the downstream application, there is still plenty of useful
 382 information at lower resolutions.

383 This experiment was run on a Dell XPS 8920 PC with Intel 4 Core i7-7700K 4.20 GHz CPU and 16 GB of
 384 RAM. The operating system was x64-bit Microsoft Windows 10 Enterprise. All manually executable applications (i.e.
 385 ignoring operating system services) were closed at the time of the experiment. Five runs were executed per resolution
 386 size and the timings averaged.

387 4.4. sradmap

388 Downstream applications of this work may need spectral radiance estimations for the entire hemispherical sky.
 389 Ideally, our models will generalize across the space between the sky samples used for machine learning. This involves
 390 some more of interpolation or scaling of outputs between the learned skeletal space provided by our ground truth

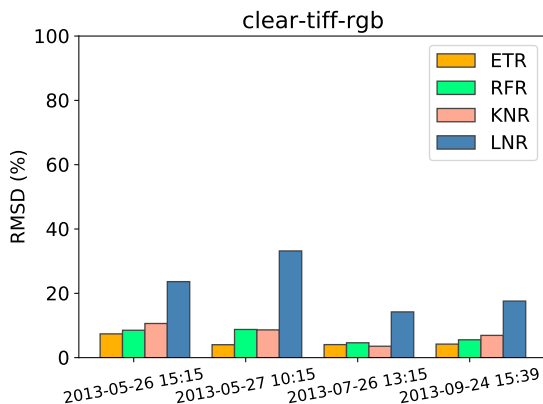


Figure 12: Model results of predicting the 81 sample point locations for each of the four holdout test skies listed in Table 1. Again, the regression models are ETR, RFR, KNR and LNR. ETR performed the best, with a total error of 4-7.5% RMSD across all 81 sample points. LNR was by far the worst performing, as expected.

391 measurements, and the entire sky. If our models do not have this ability, then usage is limited to the 81 coordinates
 392 used during measurement. Obviously the higher resolution a sky scanning pattern is, the more accurate predictions
 393 will be across the sky.

394 To provide whole sky predictions, the same input features shown in Fig. 8 can be collected for any pixel of a sky
 395 image, and then fed through a single one of our models to produce a lookup file (map) with radiance predictions per
 396 pixel. We call this resulting file a spectral radiance map (sradmap). Although the primary purpose of these files is to
 397 provide a map between pixel location and spectral radiance prediction, each prediction can be summed, normalized,
 398 and plotted against a false-color map to help visualize the topology of the data.

399 The name sradmap is an homage to radmap by Anselmo and Lauritano (2003), a supplementary tool for the daylight
 400 simulator RADIANCE (Ward, 1994). In the building performance space, our sradmap generator can be integrated into
 401 daylight simulators, energy modelers, and parametric design tools like RADIANCE, EnergyPlus (Crawley et al., 2001),
 402 SUSTAIN (Greenberg et al., 2013), and Ladybug Tools (Roudsari et al., 2013). In the computer graphics (rendering)
 403 space, sradmaps can be sampled from renderers like Mitsuba (Jakob, 2010) or Disney's Hyperion (Burley et al., 2018),
 404 for use in scenes with natural daylighting.

405 5. Results

406 Three of the four final regression models (ETR, RFR, KNR) resulted in very high R^2 scores and acceptably low
 407 RMSD error on all holdout test skies listed in Table 1. As expected, the baseline LNR model resulted in relatively poor
 408 predictions across all test skies, with an overall error of 14-24% RMSD. By contrast, ETR resulted in 4-7.5% RMSD.
 409 For test sky 07/26/2013 13:15, three of the four models predicted within 4% RMSD. In general, the tree-based models
 410 (ETR and RFR) perform better than the nearest-neighbor model (KNN). RMSD results for all models on each test sky
 411 are shown in Fig. 12. As mentioned in section Section 4, the sample azimuth feature affected results by 1-2% RMSD,
 412 but otherwise the feature scored as least important. It is possible that the deviation in results could be within any

413 Fig. 13 shows a comparison of all 81 measured and ETR predicted radiance distributions, their standard deviations,
 414 and overall averaged ratio between measured and predicted on test sky 05/27/2013 10:15. The difference in standard
 415 deviations of measured and predicted is minimal, and the averaged ratio is near 1.0 for the majority of the spectrum
 416 (350-1780 nm). Note the erratic error in the ratio graph resides within an H_2O and CO_2 absorption band, where
 417 atmospheric radiance is extremely small (Lacis and Hansen, 1974), and measurements are susceptible to noise.

418 For the same holdout test sky (05/27/2013 10:15), Fig. 14 shows ETR prediction error across the entire hemispherical
 419 sky, and highlights the two worst spectral radiance predictions (23.63% and 21% RMSD). These two measurements
 420 occur near the sun's corona, where radiance values are traditionally higher and more erratic than the rest of a clear sky.
 421 Two other predictions selected at random are shown for comparison. A vast majority of the 81 samples are predicted to
 422 within 1% RMSD. Note that even with "high" error, predicted curves align with ground truth measurements in terms

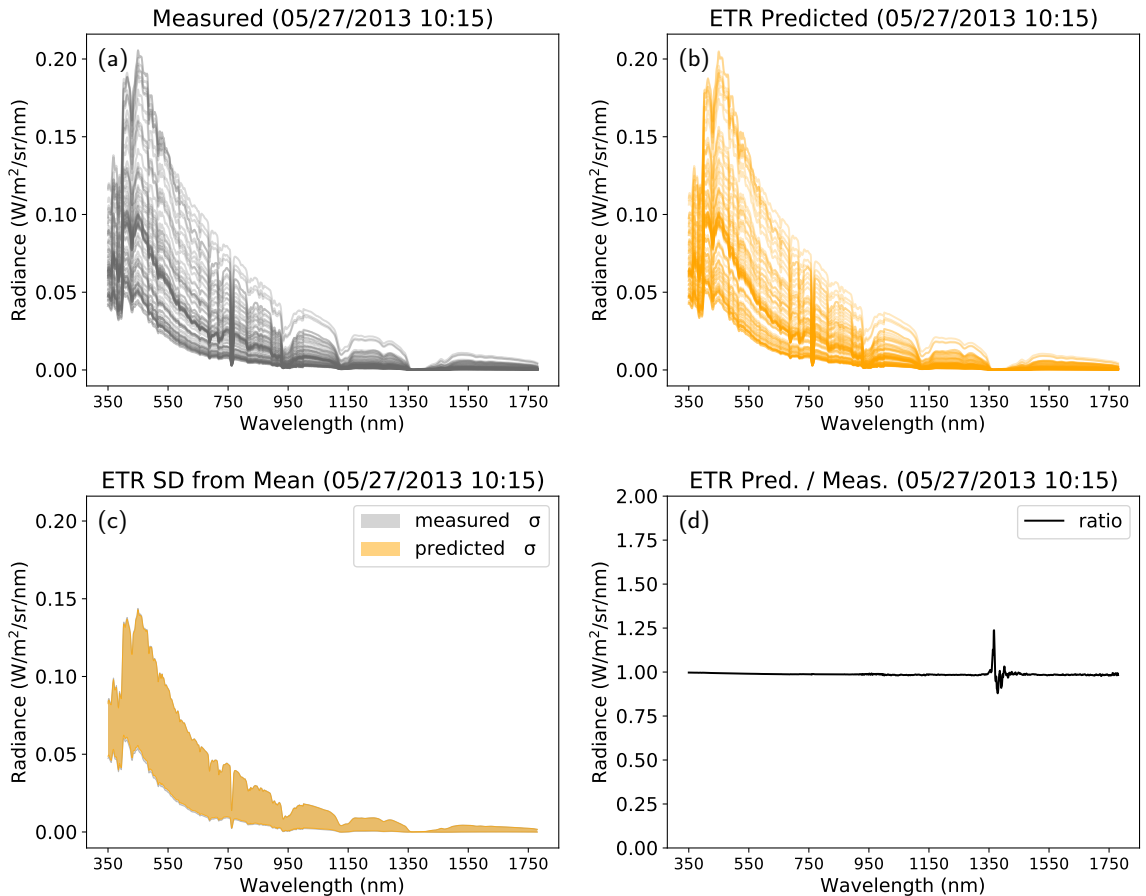


Figure 13: Whole sky results for holdout sky 05/27/2013 10:15 with ETR model. No ground truth sky samples from this capture were used for training. (a) and (b) show the 81 measured and predicted spectral radiance distributions; (c) shows the standard deviation from mean for both measured and predicted distributions; and (d) is the overall ratio between the two. Note the error in the ratio is within the absorption band near 1350 nm, where radiance is extremely small.

of shape. The models therefore have learned the wavelength relative intensities of the sky in accordance with capture time, sun location, etc. This is consistent with nearly all predicted results; while the magnitudes per wavelength sometimes deviate, the general shapes each predicted curve is accurate.

Although we were expecting some insight from providing multiple exposures of sky images, results seem to indicate that HDR data, at least for clear skies, does not improve model prediction. All HDR runs resulted in very similar error to non-HDR runs. Similarly, differences in results between 0.25 s, 1 s, and 2 s exposures were also insignificant. We believe this may be because clear sky color changes are so “uniform” throughout the day, that multiple exposures lack significance. In other words, all provided exposures may have had the same color change trends. We suspect that HDR data will be more significant in the reconstruction of spectral radiance for scattered and overcast skies, as the color variations of clouds are less uniform across exposures.

Results of our color experiment (Fig. 15) seem to indicate that color model is irrelevant to our method. This implies that our method can be used with any representation of color, as the trends in color across the sky are similar regardless of format. It is unclear if using color data initially captured in an sRGB format somehow restricted the range of the other color models after conversion. In other words, would initially capturing the sky in a color model that maps to a larger color space be better?

The results of the spectral resolution experiment (Fig. 16) show the benefits of decreasing spectral resolution from 1 to 5 nm. Model sizes (particularly the large ensemble models), as well as model training and prediction times, decrease

Real-time spectral radiance estimation of clear skies

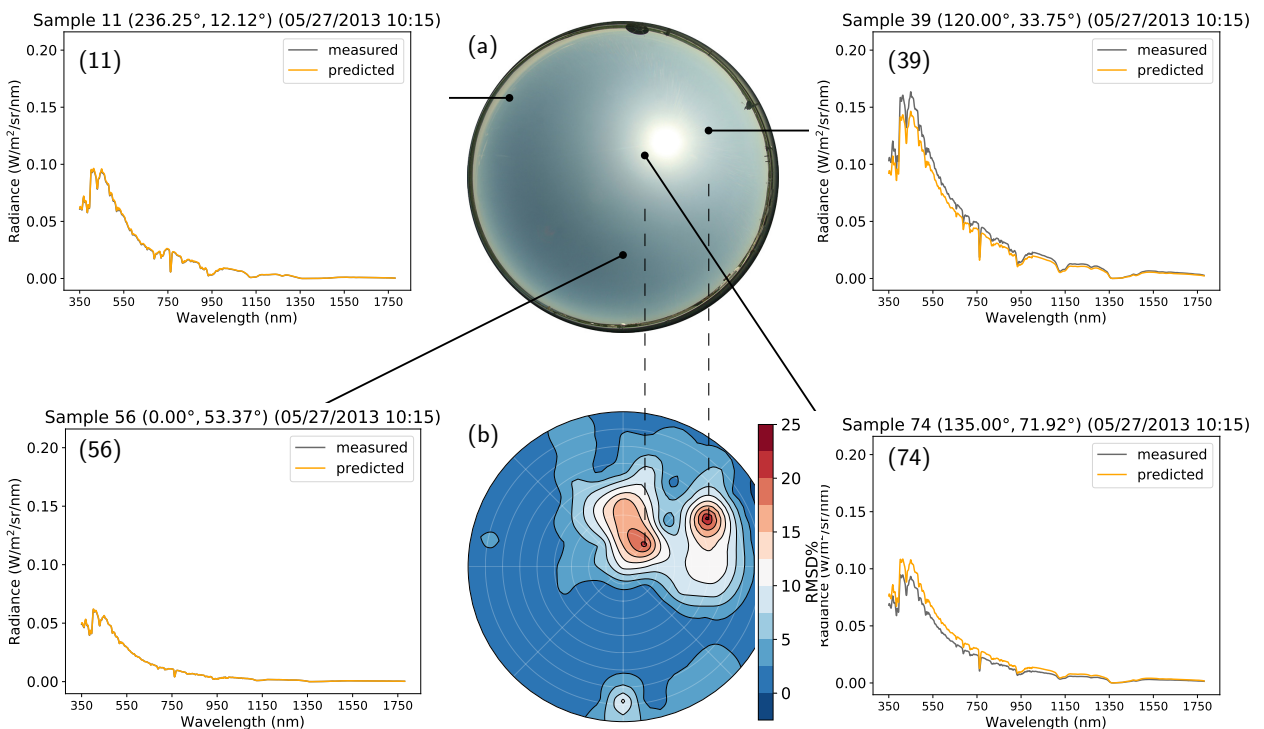


Figure 14: ETR results of four radiance predictions on holdout test sky 05/27/2013 10:15. (a) shows the camera processed JPG sky capture for convenience (the model was trained on TIFF data). (b) shows RMSD error across the entire sky. Radiance for samples (11), (56), (39) and (74) are pinpointed at their location in the sky. Samples (39) and (74) were the two worst predictions, with RMSD errors of 23.63% and 21% respectively.

440 significantly. The improvements in prediction accuracy are likely due to the radiance curve being more smooth, i.e.
 441 fewer peaks and valleys for the regression model to learn, as well as a simpler prediction problem in general, i.e. fewer
 442 outputs to predict. The size of the training dataset also decreases with reduced resolution, but that is eclipsed by the
 443 largest model sizes. Beyond 5 nm resolution, further reductions result in diminishing returns. This is an important find
 444 for real-time applications, which may operate on limited embedded hardware.

445 We note here that results between the minimally processed, uncompressed TIFF sky images and traditional, camera
 446 processed, compressed JPG sky images, were roughly the same. TIFF color data resulted in slightly better results (~1%)
 447 on some skies, though this may be within the standard deviation of prediction error and machine learning random fluc-
 448 tuation. Since the TIFF images (~35 MB) are at least 1000% larger than the JPG images (~2.5 MB) compressed with
 449 quality level 100, and the results are similar, we recommend the use of JPG images in real-time applications of our
 450 method.

451 Spectral radiance files (sradmaps) are the culminating whole sky output of our methods. They are generated by
 452 extracting features per pixel of test skies (Table 1) and feeding them through any one of our models. Linear scale false-
 453 color visualizations of ETR model predicted sradsmaps are shown in Fig. 17 and Fig. 18. Test sky images were first
 454 scaled down to a resolution of 333x333 pixels, to anticipate real-time processing speeds. sradmap generation, visualiza-
 455 tion, and logged output took ~20 s to complete on the same machine specified in Subsection 4.3; embedded hardware
 456 would likely take longer. Visualization of sradmap and logged output are not necessary for real-time applications.

457 6. Validation

458 First, no samples from our holdout test skies (Table 1), chosen at random, were used during training or preliminary
 459 testing of any model. Machine learning projects often use this method to validate a model's ability to generalize over
 460 unforeseen data. The results presented in Fig. 12, Fig. 13, and Fig. 14 show that our models have this ability. The

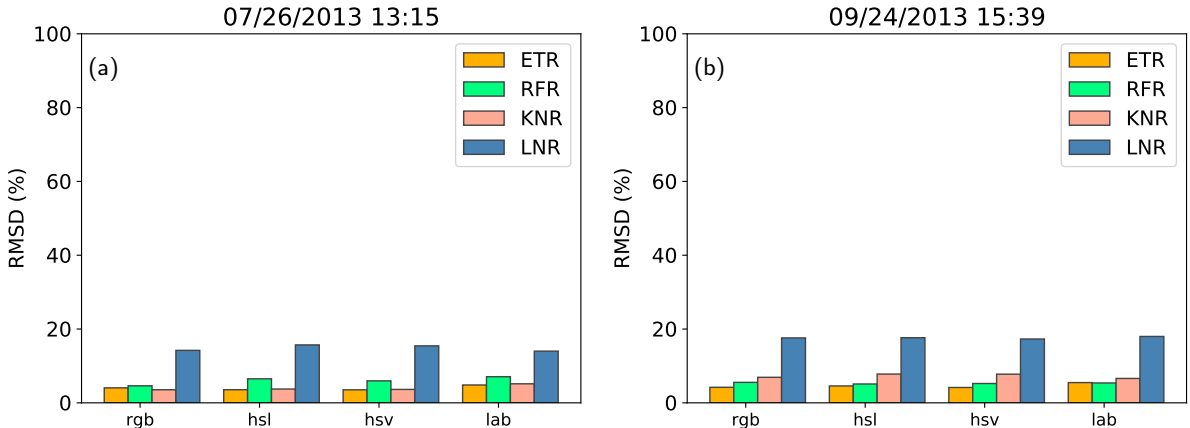


Figure 15: Sky color model made little to no difference in training and prediction results. (a) and (b) show RMSD results on 07/26/2013 13:15 and 09/24/2013 13:15 respectively.

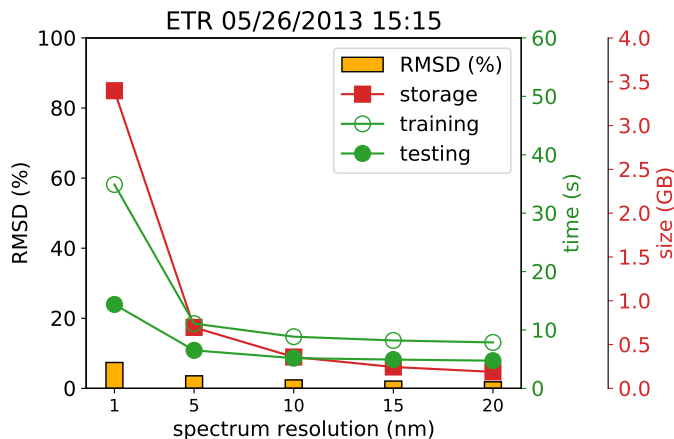


Figure 16: Limiting resolution to 5 nm drastically decreases model size, improves computation speed, and even increases prediction success, likely because the prediction problem becomes simpler with $1/5$ the number of radiance values to predict. Further reductions yield diminishing returns.

461 results of our additional experiments show that our method is robust against implementation details such as image
462 compression, exposure, and color model.

463 Next, the sradmaps presented in Fig. 17 and Fig. 18 are the result of using every pixel per test sky. These maps
464 demonstrate that our models have the ability to generalize across the entire hemisphere (i.e. predict spectral radiance
465 for every point in the sky) even when trained on a mere skeleton of samples (81 concentric 1° steradians). Note that
466 most of the sky is unaccounted for by the skeleton, including points beyond the variance of sun and sky coordinates.
467 sradmaps contain predictions for the entire sky.

468 Finally, we compare our ETR model predictions along side our ground truth measurements, with the radiance
469 distributions computed by libRadtran (Emde et al., 2016), a popular, validated radiative transfer equation (RTE) soft-
470 ware package that uses a variety of solvers developed in collaboration over decades and published in peer-reviewed
471 outlets such as: the Journal of Quantitative Spectroscopy & Radiative Transfer, Atmospheric Measuring Techniques,
472 Atmospheric Chemistry and Physics, Applied Optics, etc. MYSTIC (Buras and Mayer, 2011; Mayer, 2009; Mayer and
473 Kylling, 2005) and DISTORT (Buras and Mayer, 2011; Dahlback and Stammes, 1991; Stammes et al., 1988) are the
474 two primary comprehensive equation solvers which have been validated in multiple international model comparison
475 studies (Emde et al., 2015; Kokhanovsky et al., 2010; Cahalan et al., 2005). Since 2005, libRadtran has been cited by

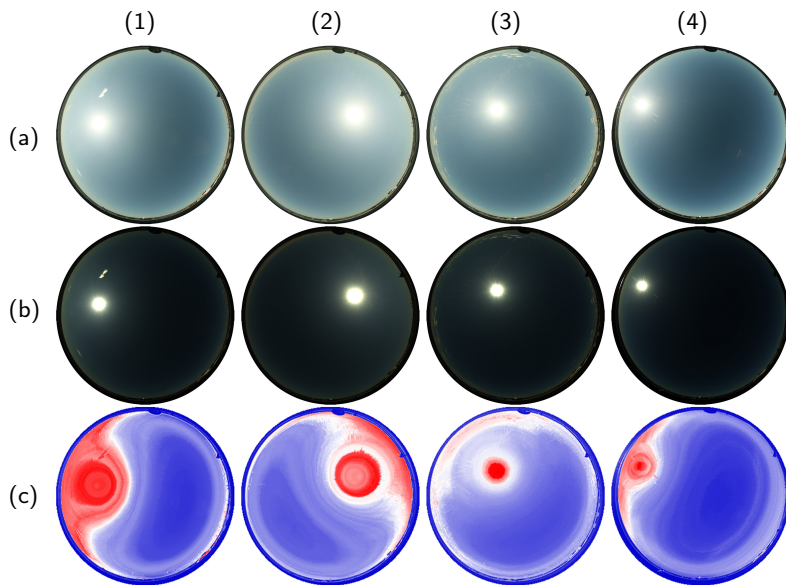


Figure 17: Columns (1-4) are the holdout test skies in Table 1, in respective order. Rows (a) and (b) show traditional, camera processed JPG and minimally processed TIFF captures, respectively. Row (c) shows the sradmap visualizations generated for skies in row (b); we use our ETR model to predict spectral radiance (350-1780 nm) for every pixel of test sky image, sum the radiance distribution, and visualize with a false-color map.

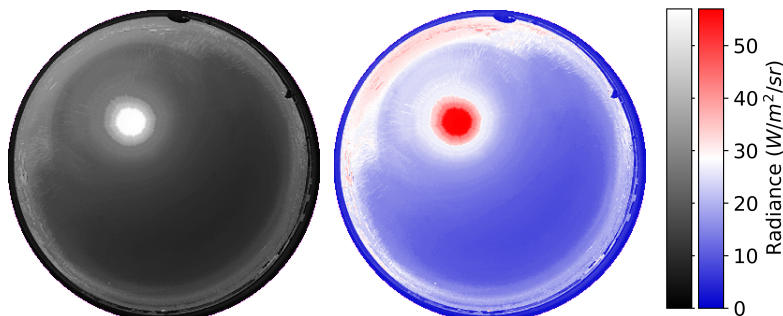


Figure 18: False-colored sradmap visualizations for holdout test sky 07/26/2013 13:15. Each pixel plotted is a summation of an entire spectral radiance distribution (350-1780 nm). There is no significance to the summation algorithm; it is simply used to visualize the data.

476 hundreds of peer-reviewed publications.

477 libRadtran was configured the same for all four holdout test skies. In other words, no sky-specific data (atmospheric
 478 measurements, aerosol databases, parameters, or ranges) were specified per test sky - we used the default configuration.
 479 Fig. 19 and Fig. 20 show that libRadtran spectral radiance for three of our four holdout test skies were in alignment
 480 with both ETR model predictions and ground truth measurements. However, for test sky 07/26/2013 13:15, libRadtran
 481 deviates from both ETR predictions and ground truth measurements (Fig. 21). All tested samples for this sky show
 482 similar deviations in magnitude, but not curve shape. As mentioned, libRadtran requires accurate atmospheric data
 483 for its calculations. Because such data was not configured, and because our predictions are closer to ground truth
 484 measurements, it is possible that our ETR model learned the sky specific atmospheric conditions libRadtran needed
 485 in order to compute accurately. In particular, we note the cirrus clouds along the horizon, which might indicate ice
 486 crystals in the atmosphere, and account for deviations between data-driven predictions and physically-based model
 487 calculations.

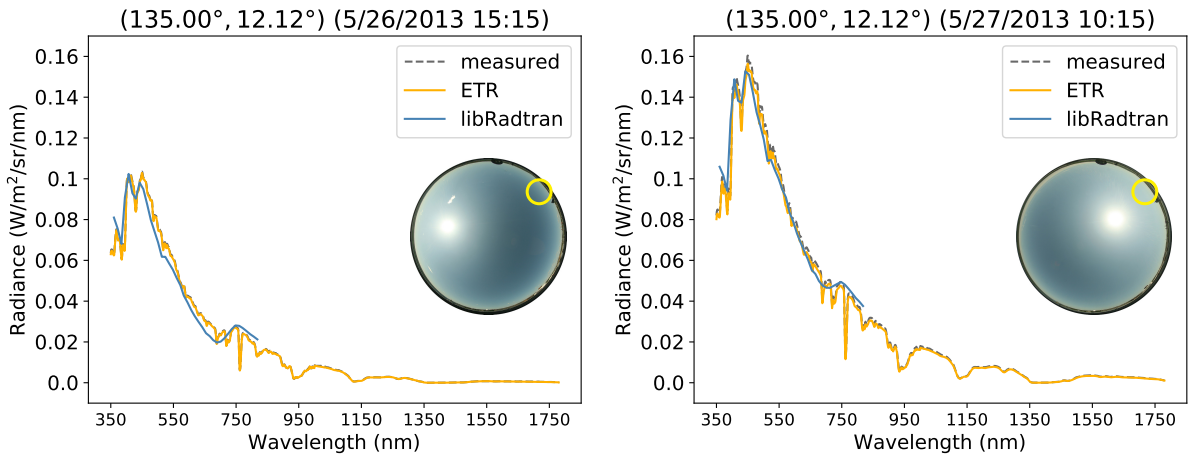


Figure 19: Spectral radiance at $(33.75^\circ$ azimuth, 12.12° altitude), circled, for two of the holdout test skies in Table 1. Spectroradiometer measurement, ETR model prediction, and libRadtran estimation plotted.

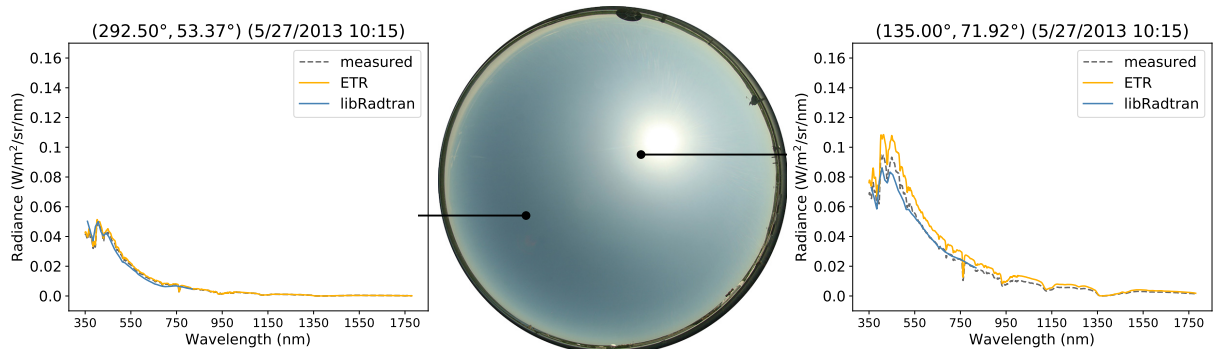


Figure 20: Spectral radiance for two sky samples of holdout test sky 05/27/2013 10:15. Spectroradiometer measurement, ETR model prediction, and libRadtran estimation plotted.

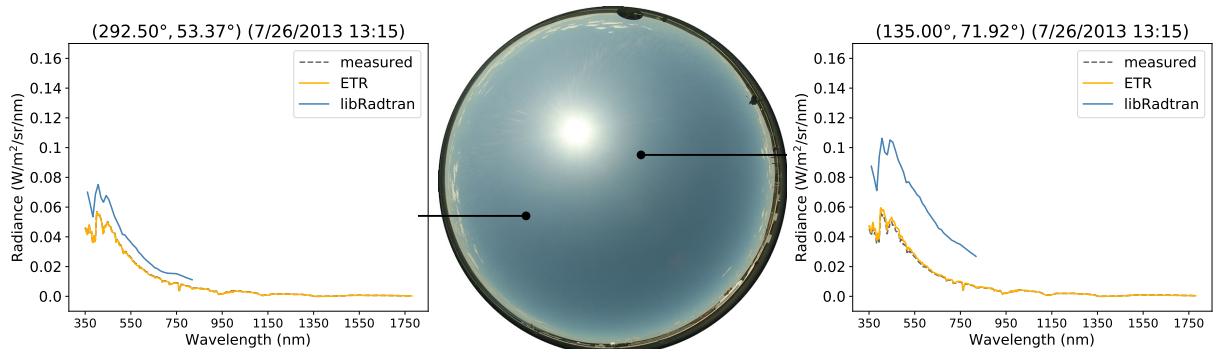


Figure 21: Spectral radiance for two sky samples of holdout test sky 07/26/2013 13:15. Spectroradiometer measurement, ETR model prediction, and libRadtran estimation plotted. libRadtran computed radiance deviates from both ETR predictions and measured ground truth data, likely because of the lack of needed atmospheric configuration data. Note the existence of cirrus clouds near the horizon.

488 **7. Conclusions**

489 Whole sky spectral radiance distributions are needed for accurate computations in a variety of applications, and yet
 490 they are often oversimplified. Real-time capable models are needed to estimate them to within acceptable tolerances.
 491 We presented a solution that: (1) took photographs of the entire hemispherical sky and measured the incoming radiance
 492 at various points, (2) used those measurements and modern machine learning methods to train regression models, and
 493 (3) used those models to predict atmospheric spectral radiance (350-1780 nm) at 1 nm resolution for the entire sky,
 494 given a photo of a clear sky and its capture timestamp, **in ~20 s of processing time, making the solution viable for real-**
 495 **time applications.** Our whole sky prediction error, for all four holdout test skies, none of which were used for training,
 496 was below 7.5% RMSD, and most of the predicted spectral radiance distributions were in line with libRadtran.

497 Our results show that image compression, color model, and exposure of clear sky imagery have little to no effect
 498 on our method. This implies that our solution is robust and less likely to be affected by implementation details. We also
 499 showed that our models have the ability to generalize across the hemispherical space between measured sky samples,
 500 allowing for atmospheric spectral radiance predictions for every point in a sky image.

501 Our trained models can be used as-is, with similarly exposed and oriented sky photos. And our methods can be
 502 reproduced to train models using new datasets. Various sky scanning systems exist which can be employed to provide
 503 regional training data. Existing correlated sky imagery and spectral radiance datasets from around the world can (and
 504 should) be used with our method. Once normalized, such comprehensive datasets could lead to even more robust
 505 models (e.g. more variations of sky turbidity). As mentioned, aerosol data can also be included as training and pre-
 506 diction features, supplied from local building sensors, GOES satellite measurements, and/or triangulated atmospheric
 507 measuring station data. Site location coordinates and/or elevation could also be investigated as input features when
 508 using multi-site data. More spectral radiance measurements within the circumsolar region would also likely improve
 509 accuracy (clear or cloudy sky), as the bulk of the energy is accounted for within that region of the sky. All research in
 510 this area could benefit by a scanning pattern that accounts for this.

511 Although many downstream applications of our research are possible, one immediately viable option is a building
 512 monitoring system equipped with all-sky camera that adjusts smart glazing and kinetic facades in response to spectral
 513 radiance across the entire non-occluded sky. Such a system would automatically harness (or attenuate) light and heat
 514 with more fine-grain control and accuracy than one that operates on a single downwelling measurement, and would be
 515 much more affordable and efficient than a live, continuously operating sky scanning system. As mentioned, various
 516 procedural processes can be applied to distinguish clear, scattered, and overcast skies, so that pixels and image regions
 517 can be passed to appropriate models for spectral radiance prediction. Cloud detection research regularly separates
 518 clear from cloudy portions of skies. We hope our research motivates the building performance community to further
 519 refine such a system. We also hope that the graphics (rendering) community notices the useful of our sradmap tool.
 520 The predicted spectral radiance distributions can and should be used in spectral renderers (the future of rendering) to
 521 provide the most accurate natural day-lighting scenes.

522 Further work will focus on scattered cloudy skies. Scattered skies account for the bulk of our publicly available
 523 dataset (63%), and in general is more complicated to model. Although our preliminary results showed that an RFR re-
 524 gression model performed moderately well on 3 our 4 test skies (Del Rocco et al., 2018), we feel that more progress can
 525 be made with more complex machine-learning techniques, such as neural networks. Simply throwing our entire dataset
 526 (clear, scattered, and overcast data) at a neural architecture search (NAS) deep learning neural network infrastructure,
 527 we achieved an 83% R^2 score, suggesting there is potential for a unified machine learned model. More investigation is
 528 needed to find the right network configuration to handle this problem. We also believe that HDR data will have more of
 529 an impact on cloudy versus clear skies, because the color gradients are not nearly as uniform. Additional work should
 530 include improving our Gaussian weighted color sampling with rectangular (as opposed to square) convolution kernels,
 531 to capture the projected solid angle area (ellipse) precisely.

532 Portions of this work were presented at SPIE Optics and Photonics for Information Processing XII (Del Rocco
 533 et al., 2018).

534 **References**

- 535 Anselmo, F., Lauritano, A., 2003. Evaluation of the solar energy potential in urban settings by irradiation map production, in: 2nd International
 536 Radiance Workshop, Radiance Community, Berkeley, California. pp. 1–1. <https://www.radiance-online.org/community/workshops/>.
- 537 Arking, A., Childs, J.D., 1985. Retrieval of cloud cover parameters from multispectral satellite images. Journal of Climate and Applied Meteorology
 538 24, 322–333.

- Berk, A., Conforti, P., Kennett, R., Perkins, T., Hawes, F., Van Den Bosch, J., 2014. MODTRAN 6: A major upgrade of the MODTRAN radiative transfer code, in: 2014 6th Workshop on Hyperspectral Image and Signal Processing: Evolution in Remote Sensing (WHISPERS), IEEE. pp. 1–4. <https://doi.org/10.1109/WHISPERS.2014.8077573>.
- Bourke, P., 2016. Lens correction and distortion. Professional web site: <http://paulbourke.net/dome/fisheyecorrect>.
- Bruneton, E., 2016. A qualitative and quantitative evaluation of 8 clear sky models. *IEEE transactions on visualization and computer graphics* 23, 2641–2655. <https://doi.org/10.1109/TVCG.2016.2622272>.
- Buras, R., Mayer, B., 2011. Efficient unbiased variance reduction techniques for monte carlo simulations of radiative transfer in cloudy atmospheres: The solution. *Journal of quantitative spectroscopy and radiative transfer* 112, 434–447.
- Burley, B., Adler, D., Chiang, M.J.Y., Driskill, H., Habel, R., Kelly, P., Kutz, P., Li, Y.K., Teece, D., 2018. The design and evolution of Disney's Hyperion renderer. *ACM Transactions on Graphics (TOG)* 37, 33. <https://doi.org/10.1145/3182159>.
- Butler, D., 2008. Architects of a low-energy future: low-and zero-energy buildings could have a huge impact on energy use and carbon emissions. we have the technologies, but if they are to mitigate climate change, green-building design must hit the mass market. *Nature* 452, 520–524.
- Cahalan, R.F., Oreopoulos, L., Marshak, A., Evans, K.F., Davis, A.B., Pincus, R., Yetzer, K.H., Mayer, B., Davies, R., Ackerman, T.P., et al., 2005. The i3rc: Bringing together the most advanced radiative transfer tools for cloudy atmospheres. *Bulletin of the American Meteorological Society* 86, 1275–1294.
- Cazorla, A., Olmo, F., Alados-Arboledas, L., 2008a. Using a sky imager for aerosol characterization. *Atmospheric Environment* 42, 2739–2745.
- Cazorla, A., Olmo, F.J., Alados-Arboledas, L., 2008b. Development of a sky imager for cloud cover assessment. *JOSA A* 25, 29–39.
- Chandrasekhar, S., 1950. Radiative Transfer. Oxford University Press.
- Chandrasekhar, S., 2013. Radiative transfer. Courier Corporation.
- Chauvin, R., Nou, J., Thil, S., Grieu, S., 2015. Modelling the clear-sky intensity distribution using a sky imager. *Solar Energy* 119, 1–17. <https://doi.org/10.1016/j.solener.2015.06.026>.
- Chen, Y., Alspaugh, S., Katz, R., 2012. Interactive analytical processing in big data systems: A cross-industry study of mapreduce workloads. arXiv preprint arXiv:1208.4174 .
- Chinchor, N., 1992. The statistical significance of the muc-4 results, in: Proceedings of the 4th conference on Message understanding, Association for Computational Linguistics. pp. 30–50.
- Cooper, W.S., 1973. On selecting a measure of retrieval effectiveness. *Journal of the American Society for Information Science* 24, 87–100.
- Cordero, R.R., Damiani, A., Ferrer, J., Rayas, J., Jorquer, J., Tobar, M., Labbe, F., Laroze, D., 2013. Downwelling and upwelling radiance distributions sampled under cloudless conditions in Antarctica. *Applied Optics* 52, 6287. URL: <https://www.osapublishing.org/abstract.cfm?URI=ao-52-25-6287>, doi:10.1364/AO.52.006287.
- Cornette, W.M., Shanks, J.G., 1992. Physically reasonable analytic expression for the single-scattering phase function. *Applied optics* 31, 3152–3160. <https://doi.org/10.1364/AO.31.003152>.
- Crawley, D.B., Lawrie, L.K., Winkelmann, F.C., Buhl, W.F., Huang, Y.J., Pedersen, C.O., Strand, R.K., Liesen, R.J., Fisher, D.E., Witte, M.J., et al., 2001. Energyplus: creating a new-generation building energy simulation program. *Energy and buildings* 33, 319–331. [https://doi.org/10.1016/S0378-7788\(00\)00114-6](https://doi.org/10.1016/S0378-7788(00)00114-6).
- Dahlback, A., Stamnes, K., 1991. A new spherical model for computing the radiation field available for photolysis and heating at twilight. *Planetary and Space Science* 39, 671–683.
- Del Rocco, J., Patterson, C.B., Dhrif, H., Kider, J.T., 2018. Learning and estimating whole sky visible, vnir, swir radiance distributions from a commercial camera, in: Optics and Photonics for Information Processing XII, SPIE. p. 107510F. <https://doi.org/10.1117/12.2321295>.
- Eltbaakh, Y.A., Ruslan, M.H., Alghoul, M., Othman, M.Y., Sopian, K., Razikov, T., 2012. Solar attenuation by aerosols: An overview. *Renewable and Sustainable Energy Reviews* 16, 4264–4276.
- Emde, C., Barlakas, V., Cornet, C., Evans, F., Korkin, S., Ota, Y., Labonne, L.C., Lyapustin, A., Macke, A., Mayer, B., et al., 2015. Iprt polarized radiative transfer model intercomparison project-phase a. *Journal of Quantitative Spectroscopy and Radiative Transfer* 164, 8–36.
- Emde, C., Buras-Schnell, R., Kylling, A., Mayer, B., Gasteiger, J., Hamann, U., Kylling, J., Richter, B., Pause, C., Dowling, T., et al., 2016. The libRadtran software package for radiative transfer calculations (version 2.0.1). *Geoscientific Model Development* , 1647–1672.
- Fisher, R., Perkins, S., Walker, A., Wolfart, E., 1996. Hypermedia image processing reference. John Wiley & Sons Ltd. <https://www.worldcat.org/title/hypermedia-image-processing-reference/oclc/43115444>.
- Gandomi, A., Haider, M., 2015. Beyond the hype: Big data concepts, methods, and analytics. *International journal of information management* 35, 137–144.
- Geurts, P., Ernst, D., Wehenkel, L., 2006. Extremely randomized trees. *Machine learning* 63, 3–42.
- Greenberg, D., Pratt, K., Hencey, B., Jones, N., Schumann, L., Dobbs, J., Dong, Z., Bosworth, D., Walter, B., 2013. Sustain: An experimental test bed for building energy simulation. *Energy and Buildings* 58, 44–57. <https://doi.org/10.1016/j.enbuild.2012.11.026>.
- Guemard, C., et al., 1995. SMARTS2 A: simple model of the atmospheric radiative transfer of sunshine: algorithms and performance assessment. Florida Solar Energy Center (FSEC) Cocoa, FL. <https://www.nrel.gov/grid/solar-resource/smarts.html>.
- Haber, J., Magnor, M., Seidel, H.P., 2005. Physically-based simulation of twilight phenomena. *ACM Transactions on Graphics (TOG)* 24, 1353–1373. <https://doi.org/10.1145/1095878.1095884>.
- Hall, M., Frank, E., Holmes, G., Pfahringer, B., Reutemann, P., Witten, I.H., 2009. The weka data mining software: an update. *ACM SIGKDD explorations newsletter* 11, 10–18. <https://doi.org/10.1145/1656274.1656278>.
- Hensen, J.L., Lamberts, R., 2012. Building performance simulation for design and operation. Routledge.
- Henyey, L.G., Greenstein, J.L., 1941. Diffuse radiation in the galaxy. *The Astrophysical Journal* 93, 70–83.
- Hess, M., Koepke, P., Schult, I., 1998. Optical properties of aerosols and clouds: The software package opac. *Bulletin of the American meteorological society* 79, 831–844.
- Hoerl, A.E., Kennard, R.W., 1970. Ridge regression: Biased estimation for nonorthogonal problems. *Technometrics* 12, 55–67.
- Holben, B.N., Eck, T.F., Slutsker, I., Tanre, D., Buis, J., Setzer, A., Vermote, E., Reagan, J.A., Kaufman, Y., Nakajima, T., et al., 1998. Aeronet—a

- federated instrument network and data archive for aerosol characterization. *Remote sensing of environment* 66, 1–16.
- Hosek, L., Wilkie, A., 2012. An analytic model for full spectral sky-dome radiance. *ACM Transactions on Graphics (TOG)* 31, 95. <https://doi.org/10.1145/2185520.2185591>.
- Igawa, N., Nakamura, H., 2001. All sky model as a standard sky for the simulation of daylit environment. *Building and Environment* 36, 763–770. [https://doi.org/10.1016/S0360-1323\(00\)00062-7](https://doi.org/10.1016/S0360-1323(00)00062-7).
- Iqbal, M., 2012. An introduction to solar radiation. Elsevier.
- Jakica, N., 2017. State-of-the-art review of solar design tools and methods for assessing daylighting and solar potential for building-integrated photovoltaics. *Renewable and Sustainable Energy Reviews* .
- Jakob, W., 2010. Mitsuba renderer. <Http://www.mitsuba-renderer.org>.
- Jarosz, W., 2008. Efficient Monte Carlo methods for light transport in scattering media. Citeseer.
- Joblove, G.H., Greenberg, D., 1978. Color spaces for computer graphics, in: *ACM SIGGRAPH Computer Graphics*, ACM. pp. 20–25. <https://doi.org/10.1145/965139.807362>.
- Kajiya, J.T., 1986. The rendering equation, in: *ACM SIGGRAPH computer graphics*, ACM. pp. 143–150. <https://doi.org/10.1145/15886.15902>.
- Kider, J.T., Knowlton, D., Newlin, J., Li, Y.K., Greenberg, D.P., 2014. A framework for the experimental comparison of solar and skydome illumination. *ACM Transactions on Graphics (TOG)* 33, 180. <https://doi.org/10.1145/2661229.2661259>.
- Kinney, J.A.S., 1958. Comparison of scotopic, mesopic, and photopic spectral sensitivity curves. *JOSA* 48, 185–190. <https://doi.org/10.1364/JOSA.48.000185>.
- Kittler, R., 1994. Some qualities of scattering functions defining sky radiance distributions. *Solar Energy* 53, 511–516. [https://doi.org/10.1016/0038-092X\(94\)90131-K](https://doi.org/10.1016/0038-092X(94)90131-K).
- Kocev, D., Vens, C., Struyf, J., Džeroski, S., 2013. Tree ensembles for predicting structured outputs. *Pattern Recognition* 46, 817–833.
- Kocifaj, M., 2009. Sky luminance/radiance model with multiple scattering effect. *Solar Energy* 83, 1914–1922. <https://doi.org/10.1016/j.solener.2009.07.004>.
- Kocifaj, M., 2012. Angular distribution of scattered radiation under broken cloud arrays: an approximation of successive orders of scattering. *Solar Energy* 86, 3575–3586. <https://doi.org/10.1016/j.solener.2012.06.022>.
- Kocifaj, M., 2015. Unified model of radiance patterns under arbitrary sky conditions. *Solar Energy* 115, 40–51. <http://linkinghub.elsevier.com/retrieve/pii/S0038092X15000894>.
- Koenderink, J.J., 2010. *Color for the Sciences*. The MIT Press.
- Kohavi, R., et al., 1995. A study of cross-validation and bootstrap for accuracy estimation and model selection, in: *Ijcai*, Montreal, Canada. pp. 1137–1145.
- Kokhanovsky, A.A., Budak, V.P., Cornet, C., Duan, M., Emde, C., Katsev, I.L., Klyukov, D.A., Korkin, S.V., C-Labonnote, L., Mayer, B., et al., 2010. Benchmark results in vector atmospheric radiative transfer. *Journal of Quantitative Spectroscopy and Radiative Transfer* 111, 1931–1946.
- Kylling, A., Stamnes, K., Tsay, S.C., 1995. A reliable and efficient two-stream algorithm for spherical radiative transfer: Documentation of accuracy in realistic layered media. *Journal of Atmospheric Chemistry* 21, 115–150.
- Lacis, A.A., Hansen, J., 1974. A parameterization for the absorption of solar radiation in the earth's atmosphere. *Journal of the atmospheric sciences* 31, 118–133. [https://doi.org/10.1175/1520-0469\(1974\)031%3C0118:APFTA0%3E2.0.CO;2](https://doi.org/10.1175/1520-0469(1974)031%3C0118:APFTA0%3E2.0.CO;2).
- Laney, D., 2001. 3d data management: Controlling data volume, velocity and variety. *META group research note* 6, 1.
- Lee Jr, R.L., 2008. Measuring overcast colors with all-sky imaging. *Applied optics* 47, H106–H115.
- Li, Q., Lu, W., Yang, J., 2011. A hybrid thresholding algorithm for cloud detection on ground-based color images. *Journal of atmospheric and oceanic technology* 28, 1286–1296.
- LibRaw, 2018. libraw, raw image decoder. <Http://www.libraw.org>.
- Littlefair, P.J., 1981. The luminance distribution of an average sky. *Lighting Research & Technology* 13, 192–198. <https://doi.org/10.1177/09603271801300402>.
- López-Álvarez, M.A., Hernández-Andrés, J., Romero, J., Olmo, F.J., Cazorla, A., Alados-Arboledas, L., 2008. Using a trichromatic CCD camera for spectral skylight estimation. *Applied optics* 47, H31–H38. URL: <Https://www.osapublishing.org/abstract.cfm?uri=ao-47-34-h31>.
- Macskassy, S.A., Hirsh, H., 2003. Adding numbers to text classification, in: *Proceedings of the twelfth international conference on Information and knowledge management*, ACM. pp. 240–246. <https://doi.org/10.1145/956863.956910>.
- Malthus, T., MacLellan, C., 2010. High performance fore optic accessories and tools for reflectance and radiometric measurements with the ASD FR3 spectroradiometer, in: *ESA Hyperspectral Workshop 2010 “From Chris/Proba to PRISMA and EnMAP and beyond”*, European Space Agency. p. EP101432. <Http://hdl.handle.net/102.100.100/108223>.
- Mayer, B., 2009. Radiative transfer in the cloudy atmosphere, in: *EPJ Web of Conferences*, EDP Sciences. pp. 75–99.
- Mayer, B., Kylling, A., 2005. The libRadtran software package for radiative transfer calculations. *Atmospheric Chemistry and Physics* 5, 1855–1877.
- Mazria, E., Kershner, K., 2008. Meeting the 2030 challenge through building codes. *Architecture 2030*.
- Mie, G., 1908. Beiträge zur optik trüber medien, speziell kolloidalen metallösungen. *Annalen der physik* 330, 377–445.
- Mishchenko, M.I., Travis, L.D., Lacis, A.A., 2002. Scattering, absorption, and emission of light by small particles. Cambridge university press.
- Nakamura, H., Oki, M., Hayashi, Y., 1985. A study on the estimation of the relative frequency of occurrences of the clear sky, the intermediate sky and the overcast sky in japan. *Journal of Light & Visual Environment* 9, 2_22–2_31. Https://doi.org/10.2150/jlve.9.2_22.
- Nishita, T., Dobashi, Y., Nakamae, E., 1996. Display of clouds taking into account multiple anisotropic scattering and sky light, in: *Proceedings of the 23rd annual conference on Computer graphics and interactive techniques*, ACM. pp. 379–386. <Https://doi.org/10.1145/237170.237277>.
- Nishita, T., Sirai, T., Nakamae, E., Tadamura, K., 1993. Display of the earth taking into account atmospheric scattering, in: *SIGGRAPH*, p. 175. <Https://doi.org/10.1145/166117.166140>.
- Nou, J., Chauvin, R., Eynard, J., Thil, S., Grieu, S., 2018. Towards the intrahour forecasting of direct normal irradiance using sky-imaging data.

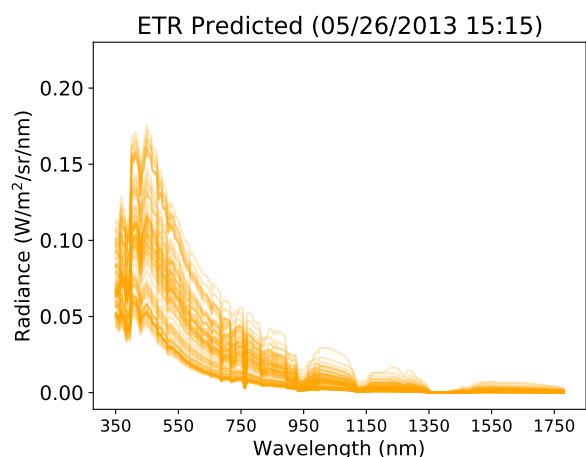
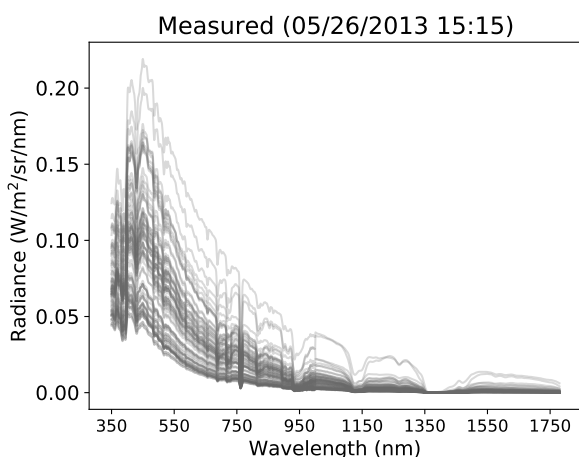
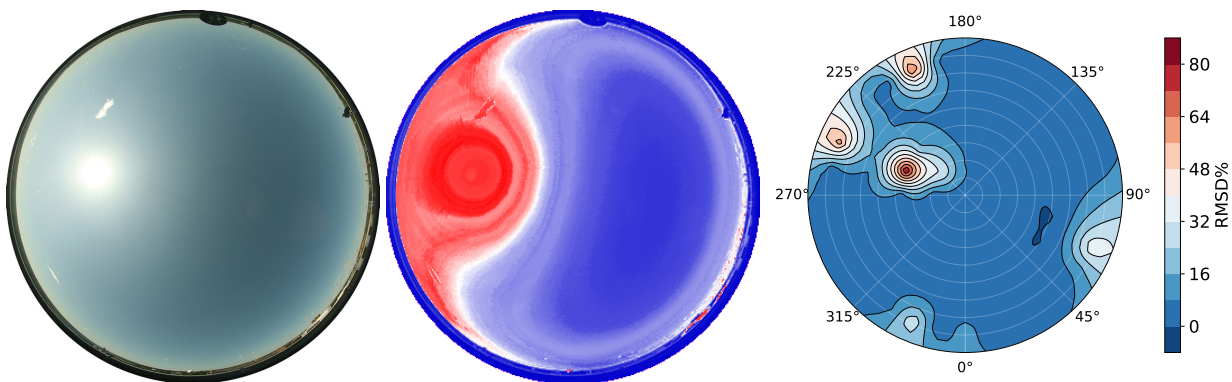
- 665 Heliyon 4, e00598. <https://doi.org/10.1016/j.heliyon.2018.e00598>.
- 666 Office Of The Federal Coordinator For Meteorological Services And Supporting Research, 2017. Chapter 9: Sky Condition, in: Federal Meteo-
667 rological Handbook No. 1: Surface Weather Observations and Reports. fcm-h1-2017 ed.. National Oceanic and Atmospheric Administration,
668 Washington, D.C., pp. 45–50. URL: https://www.ofcm.gov/publications/fmh/FMH1/FMH1_2017.pdf.
- 669 Parker, J.R., 2010. Algorithms for image processing and computer vision. John Wiley & Sons. <https://www.worldcat.org/title/algorithms-for-image-processing-and-computer-vision/oclc/813666888>.
- 670 Pedregosa, F., Varoquaux, G., Gramfort, A., Michel, V., Thirion, B., Grisel, O., Blondel, M., Prettenhofer, P., Weiss, R., Dubourg, V., et al., 2011.
671 Scikit-learn: Machine learning in python. Journal of machine learning research 12, 2825–2830.
- 672 Perez, R., Seals, R., Michalsky, J., 1993. All-weather model for sky luminance distribution—preliminary configuration and validation. Solar energy
673 50, 235–245. [https://doi.org/10.1016/0038-092X\(93\)90017-I](https://doi.org/10.1016/0038-092X(93)90017-I).
- 674 Picard, R.R., Cook, R.D., 1984. Cross-validation of regression models. Journal of the American Statistical Association 79, 575–583. <https://doi.org/10.1080/01621459.1984.10478083>.
- 675 Pokrowski, G., 1929. Über einen scheinbaren mie-effekt und seine mögliche rolle in der atmosphärenoptik. Zeitschrift für Physik 53, 67–71.
- 676 Poynton, C.A., 1995. A guided tour of colour space, in: New Foundation for Video Technology: The SMPTE Advanced Television and Electronic
677 Imaging Conference, SMPTE. pp. 167–180. <https://doi.org/10.5594/M00840>.
- 678 Preetham, A., Shirley, P., Smits, B., 1999. A practical analytic model for daylight, in: Proceedings of the 26th Annual Conference on Computer
679 Graphics and Interactive Techniques, ACM. ACM Press/Addison-Wesley Publishing Co.. pp. 91–100. <https://doi.org/10.1145/311535.311545>.
- 680 Reda, I., Andreas, A., 2004. Solar position algorithm for solar radiation applications. Solar energy 76, 577–589. <https://doi.org/10.1016/j.solener.2003.12.003>.
- 681 Ricchiazzi, P., Yang, S., Gautier, C., Sowle, D., 1998. Sbdart: A research and teaching software tool for plane-parallel radiative transfer in the earth's
682 atmosphere. Bulletin of the American Meteorological Society 79, 2101–2114. [https://doi.org/10.1175/1520-0477\(1998\)079<2101:SARATS>2.0.CO;2](https://doi.org/10.1175/1520-0477(1998)079<2101:SARATS>2.0.CO;2).
- 683 Riechert, M., 2018. rawpy (0.13.1), RAW image processing for Python. <https://pypi.org/project/rawpy>.
- 684 Robertson, A.R., et al., 1977. The CIE 1976 color-difference formulae. Color Research & Application 2, 7–11. <https://doi.org/10.1002/j.1520-6378.1977.tb00104.x>.
- 685 Roudsari, M.S., Pak, M., Smith, A., et al., 2013. Ladybug: A parametric environmental plugin for Grasshopper to help designers create an
686 environmentally-conscious design, in: Proceedings of the 13th international IBPSA conference held in Lyon, France Aug, pp. 3128–3135.
687 https://www.ibpsa.org/proceedings/bs2013/p_2499.pdf.
- 688 Sagiroglu, S., Sinanc, D., 2013. Big data: A review, in: 2013 international conference on collaboration technologies and systems (CTS), IEEE. pp.
689 42–47.
- 690 Saito, M., Iwabuchi, H., 2016. Cloud Discrimination from Sky Images Using a Clear-Sky Index. Journal of Atmospheric and Oceanic Technology
691 33, 1583–1595. URL: <http://journals.ametsoc.org/doi/10.1175/JTECH-D-15-0204.1>, doi:10.1175/JTECH-D-15-0204.1.
- 692 Saito, M., Iwabuchi, H., Murata, I., 2016. Estimation of spectral distribution of sky radiance using a commercial digital camera. Applied Optics
693 55, 415. <https://doi.org/10.1364/AO.55.000415>.
- 694 Sasaki, Y., 2007. The truth oh the f-measure. Technical Report, Version: 26th .
- 695 Satylmys, P., Bashford-Rogers, T., Chalmers, A., Debattista, K., 2016. A machine-learning-driven sky model. IEEE computer graphics and
696 applications 37, 80–91. <https://doi.org/10.1109/MCG.2016.67>.
- 697 Sigernes, F., Holmes, J.M., Dyrland, M., Lorentzen, D.A., Svenøe, T., Heia, K., Aso, T., Chernouss, S., Deehr, C.S., 2008. Sensitivity calibration
698 of digital colour cameras for auroral imaging. Optics express 16, 15623–15632.
- 699 Smith, A.R., 1978. Color gamut transform pairs. ACM SIGGRAPH Computer Graphics 12, 12–19. <https://doi.org/10.1145/965139.807361>.
- 700 Smith, C.J., Forster, P.M., Crook, R., 2016. An all-sky radiative transfer method to predict optimal tilt and azimuth angle of a solar collector. Solar
701 Energy 123, 88–101.
- 702 Stammes, K., Tsay, S.C., Wiscombe, W., Jayaweera, K., 1988. Numerically stable algorithm for discrete-ordinate-method radiative transfer in
703 multiple scattering and emitting layered media. Applied optics 27, 2502–2509.
- 704 Stokes, M., Anderson, M., Chandrasekar, S., Motta, R., 1996. A standard default color space for the internet-sRGB. Microsoft and Hewlett-Packard
705 Joint Report <https://www.w3.org/Graphics/Color/sRGB>.
- 706 Stone, E., 2015. Completely painless programmer's guide to XYZ, RGB, ICC, xyY, and TRCs. Personal website <https://ninedegreesbelow.com/photography/xyz-rgb.html>.
- 707 Strutt, J.W., 1871. On the light from the sky, its polarization and colour. The London, Edinburgh, and Dublin Philosophical Magazine and Journal
708 of Science 41, 107–120.
- 709 Stumpfel, J., Tchou, C., Jones, A., Hawkins, T., Wenger, A., Debevec, P., 2004. Direct hdr capture of the sun and sky, in: Proceedings of the 3rd
710 International Conference on Computer Graphics, Virtual Reality, Visualisation and Interaction in Africa, ACM. pp. 145–149. <http://doi.acm.org/10.1145/1029949.1029977>.
- 711 Tibshirani, R., 1996. Regression shrinkage and selection via the lasso. Journal of the Royal Statistical Society. Series B (Methodological) , 267–288.
- 712 Tohsing, K., Schrempf, M., Riechelmann, S., Seckmeyer, G., 2014. Validation of spectral sky radiance derived from all-sky camera images-a case
713 study. Atmospheric Measurement Techniques 7 (2014), Nr. 7. <https://doi.org/10.15488/5>.
- 714 Van Rijsbergen, C., 1979. Information Retrieval. Butterworths.
- 715 Vermote, E., Tanré, D., Deuzé, J., Herman, M., Morcrette, J., Kotchenova, S., 2006. Second simulation of a satellite signal in the solar spectrum-
716 vector (6SV). 6S User Guide Version 3, 1–55.
- 717 Ward, G.J., 1994. The RADIANCE lighting simulation and rendering system, in: Proceedings of the 21st annual conference on Computer graphics
718 and interactive techniques, ACM. pp. 459–472. <https://doi.org/10.1145/192161.192286>.

- 728 Wright, W.D., 1929. A re-determination of the trichromatic coefficients of the spectral colours. *Transactions of the Optical Society* 30, 141.
729 <https://doi.org/10.1088/1475-4878/30/4/301>.
- 730 Yamashita, M., Yoshimura, M., Nakashizuka, T., 2004. Cloud cover estimation using multitemporal hemisphere imageries. *International Archives
731 of Photogrammetry Remote Sensing and Spatial Information Sciences* 35, 826–829.
- 732 Yao, W., Li, Z., Zhao, Q., Lu, Y., Lu, R., 2015. A new anisotropic diffuse radiation model. *Energy Conversion and Management* 95, 304–313.
733 <https://doi.org/10.1016/j.enconman.2015.01.016>.
- 734 Yu, C.H., 1977. Exploratory data analysis. *Methods* 2, 131–160. <https://dx.doi.org/10.1093/obo/9780199828340-0200>.
- 735 Zotti, G., Wilkie, A., Purgathofer, W., 2007. A critical review of the preetham skylight model, in: *WSCG '2007: Short Communications Proceedings*,
736 Václav Skala-UNION Agency. pp. 23–30. <http://hdl.handle.net/11025/11160>.
- 737 Zou, H., Hastie, T., 2005. Regularization and variable selection via the elastic net. *Journal of the Royal Statistical Society: Series B (Statistical
738 Methodology)* 67, 301–320.
- 739

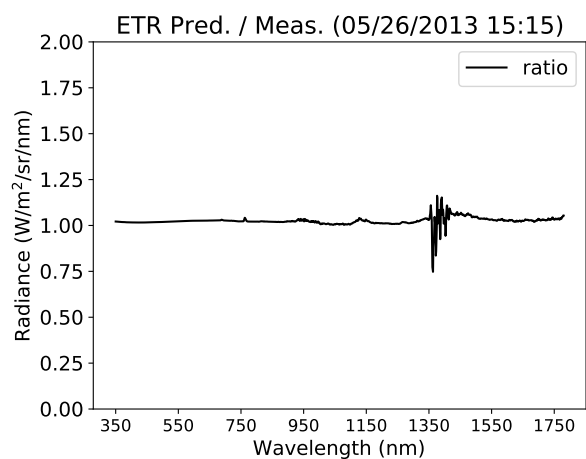
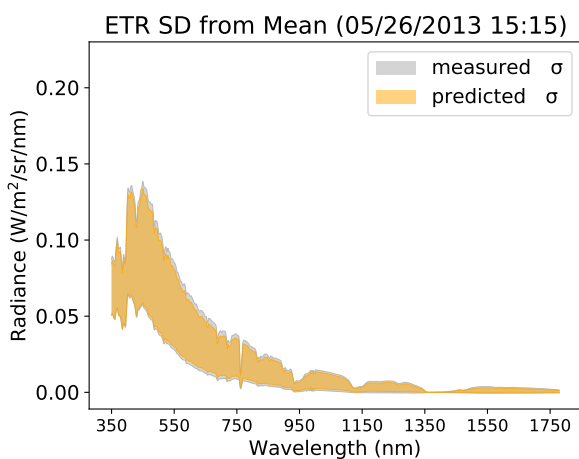
740 Appendix A - 05/26/13 15:15³

741 Whole sky ETR predictions for holdout test sky 05/26/2013 15:15.

742



744



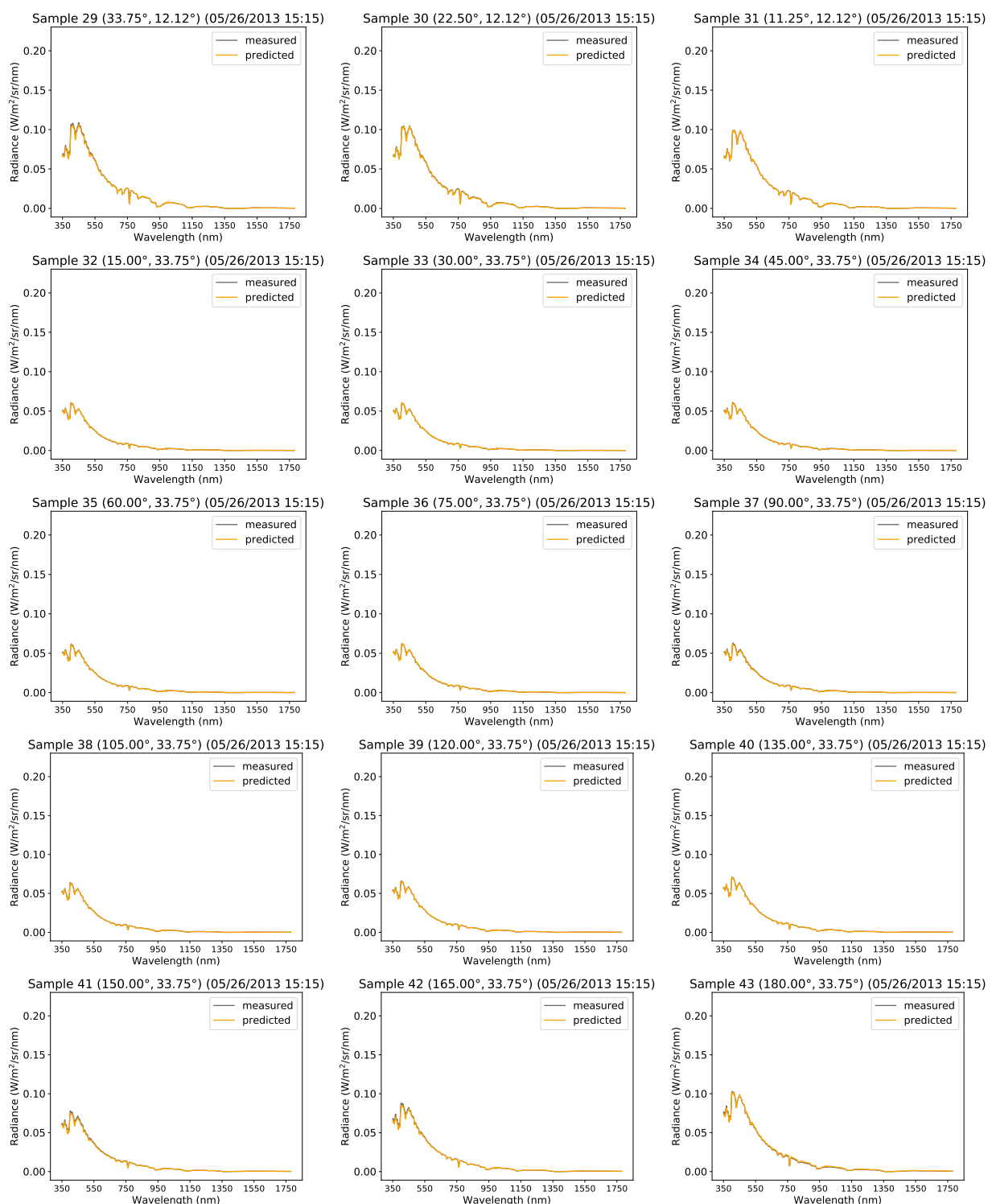
745

³Provided for reviewing purposes only.

Real-time spectral radiance estimation of clear skies

746 15 of 81 consecutive ETR spectral radiance predictions for holdout test sky 05/26/2013 15:15.

747



748

749

750

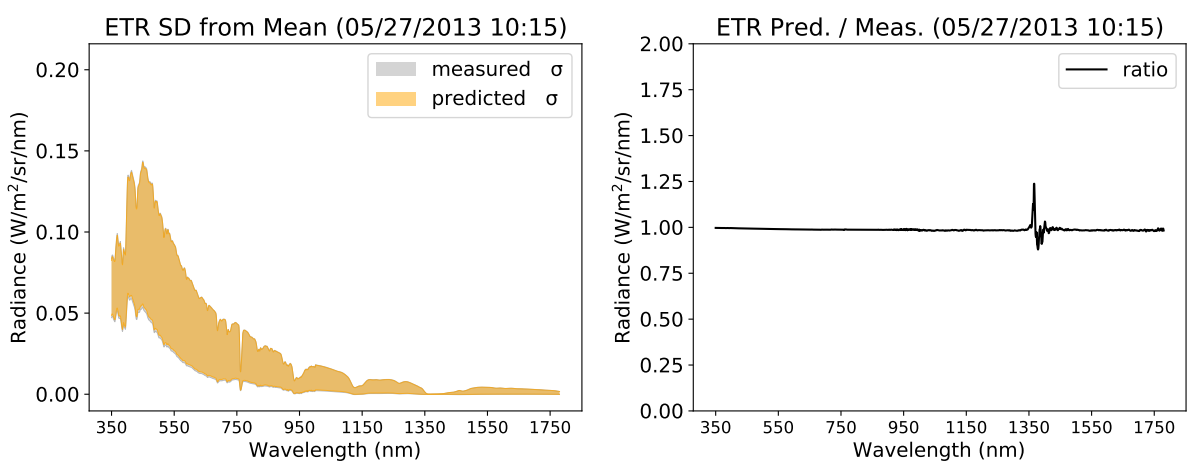
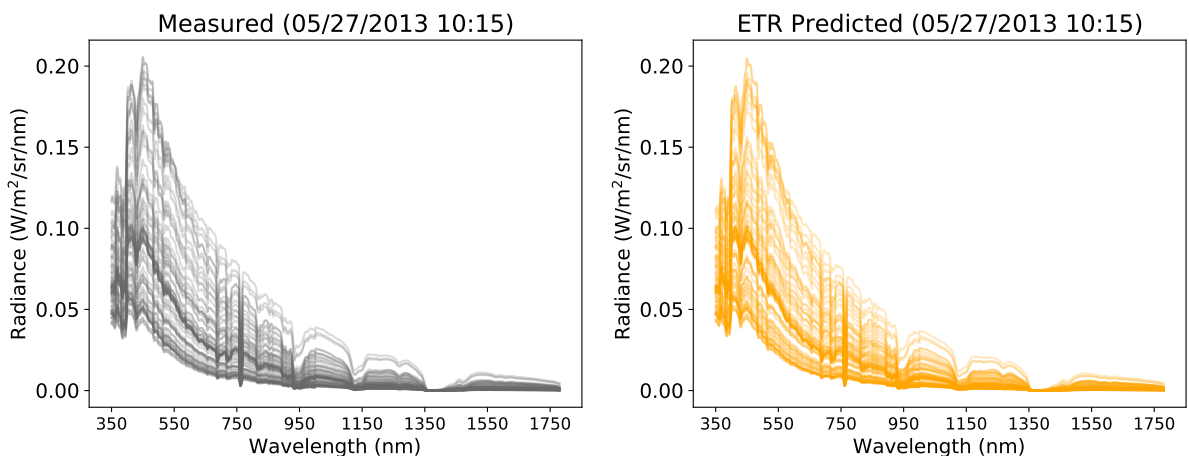
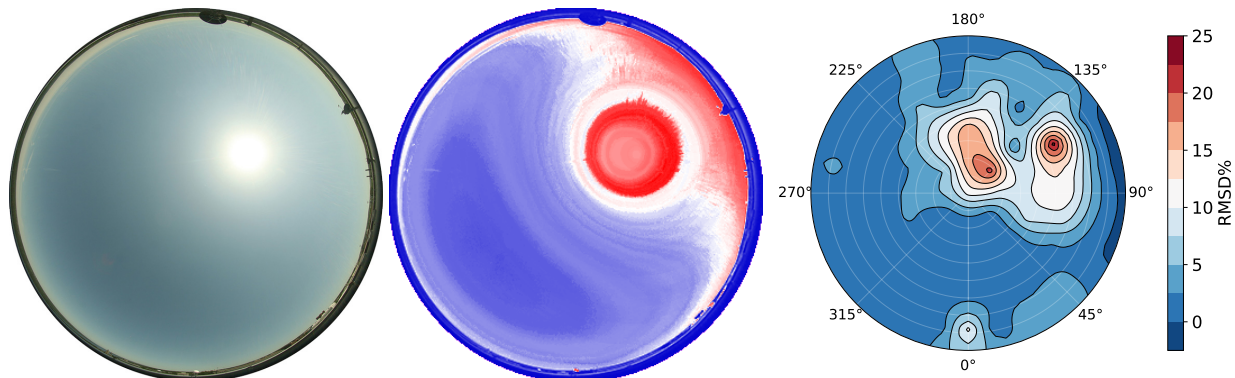
751

752

753

754 Appendix B - 05/27/13 10:15⁴

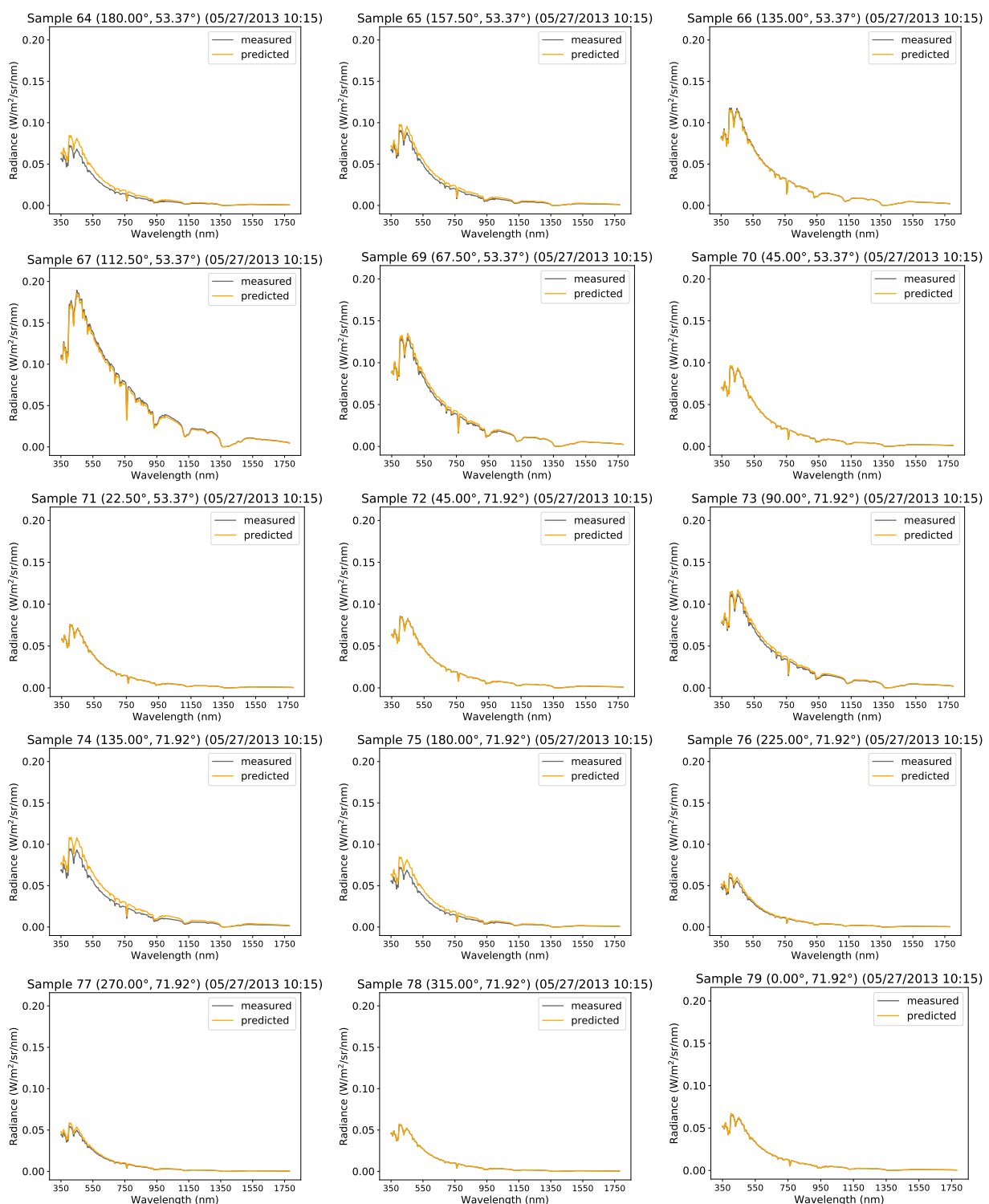
755 Whole sky ETR predictions for holdout test sky 05/27/2013 10:15.

⁴Provided for reviewing purposes only.

Real-time spectral radiance estimation of clear skies

759 15 of 81 consecutive ETR spectral radiance predictions for holdout test sky 05/27/2013 10:15.

760



761

762

763

764

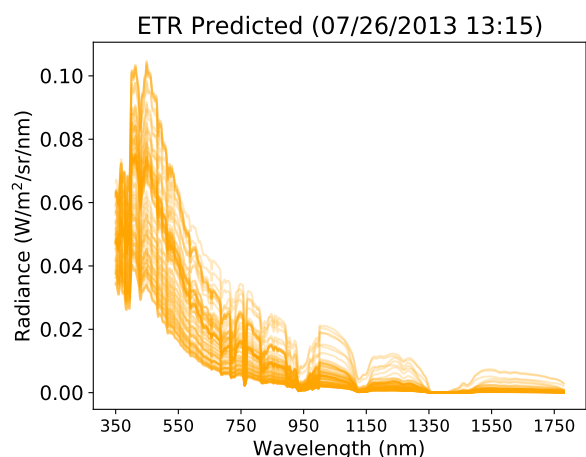
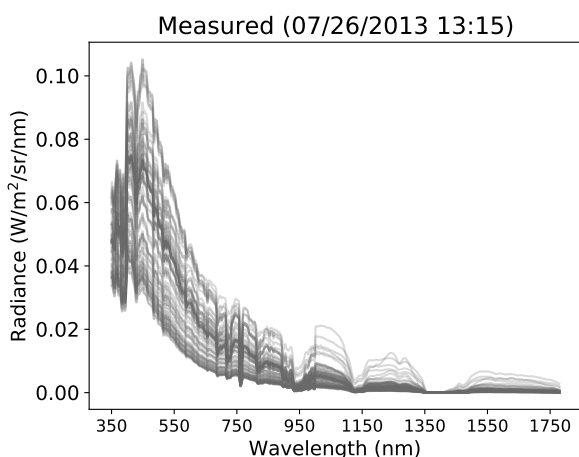
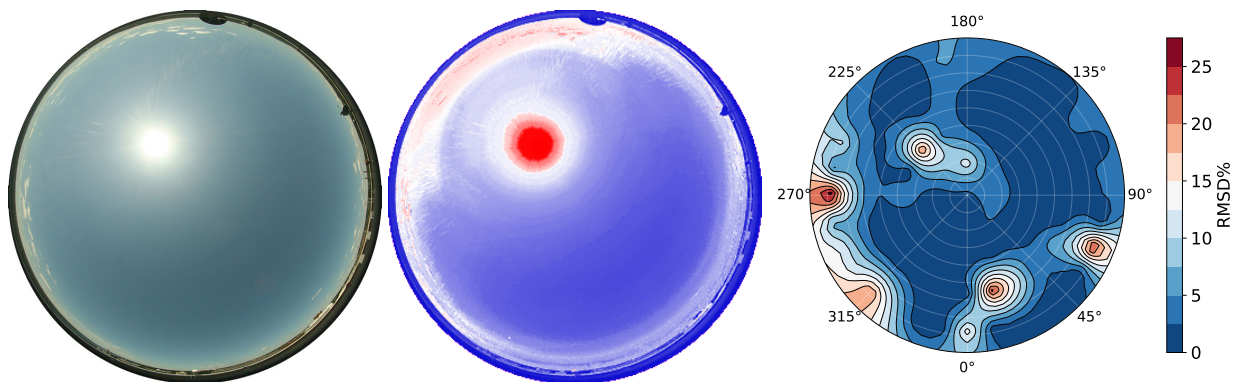
765

766

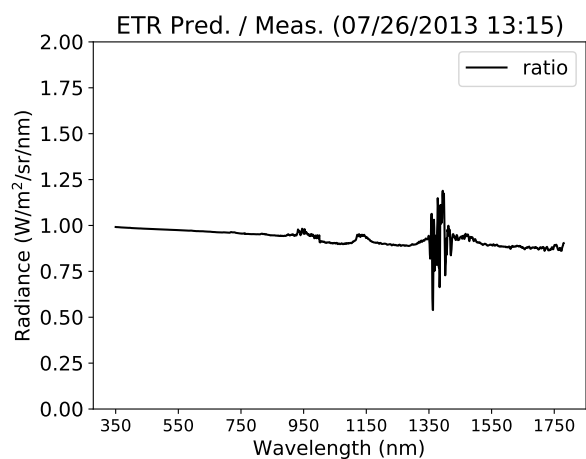
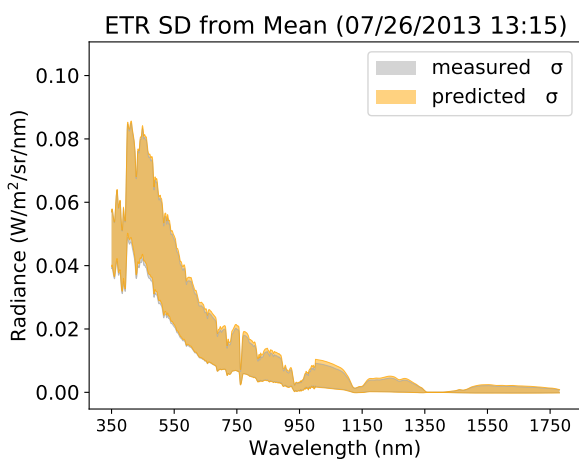
767 Appendix C - 07/26/13 13:15⁵

768 Whole sky ETR predictions for holdout test sky 07/26/2013 13:15.

769



771



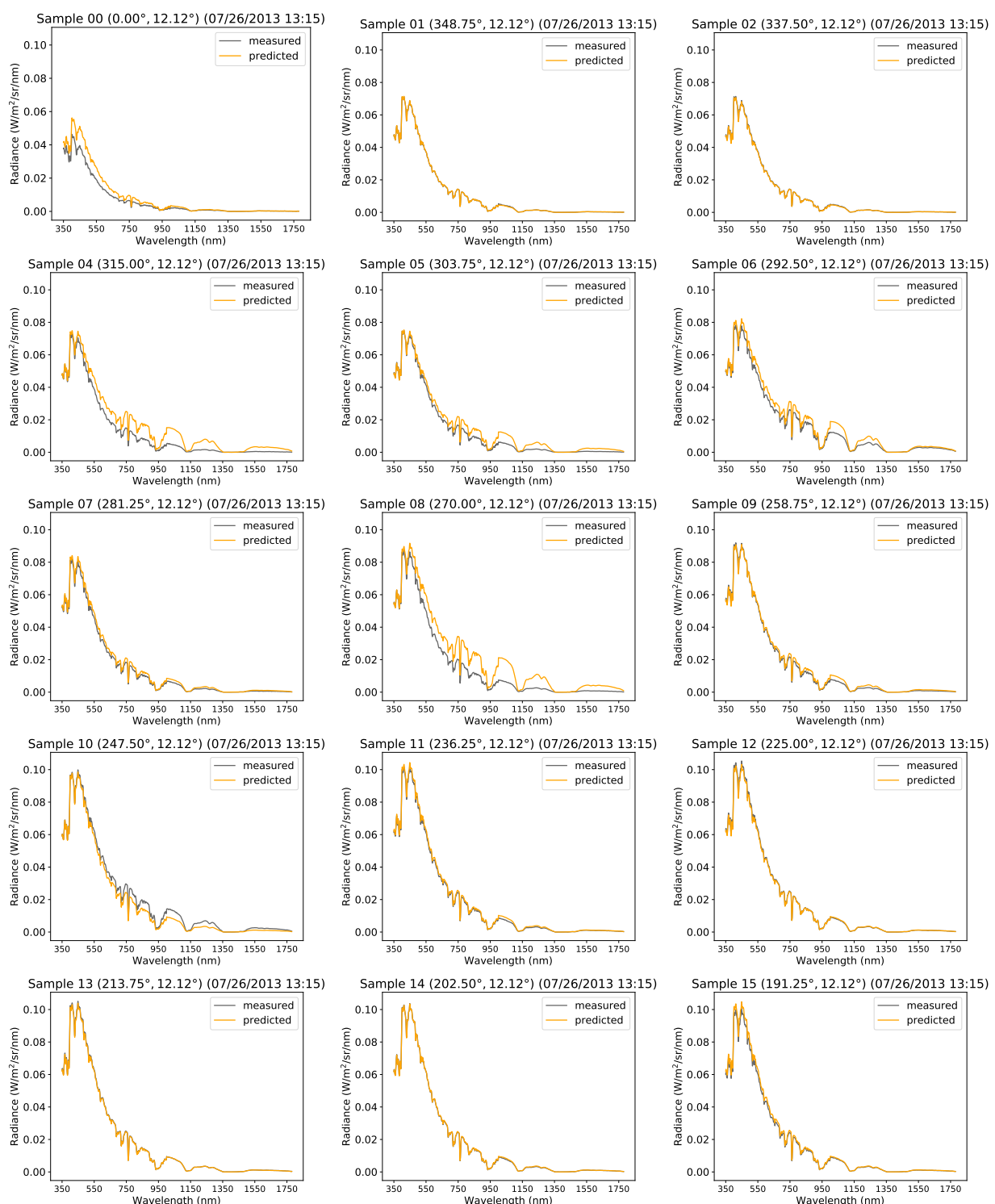
772

⁵Provided for reviewing purposes only.

Real-time spectral radiance estimation of clear skies

773 15 of 81 consecutive ETR spectral radiance predictions for holdout test sky 07/26/2013 13:15.

774



775

776

777

778

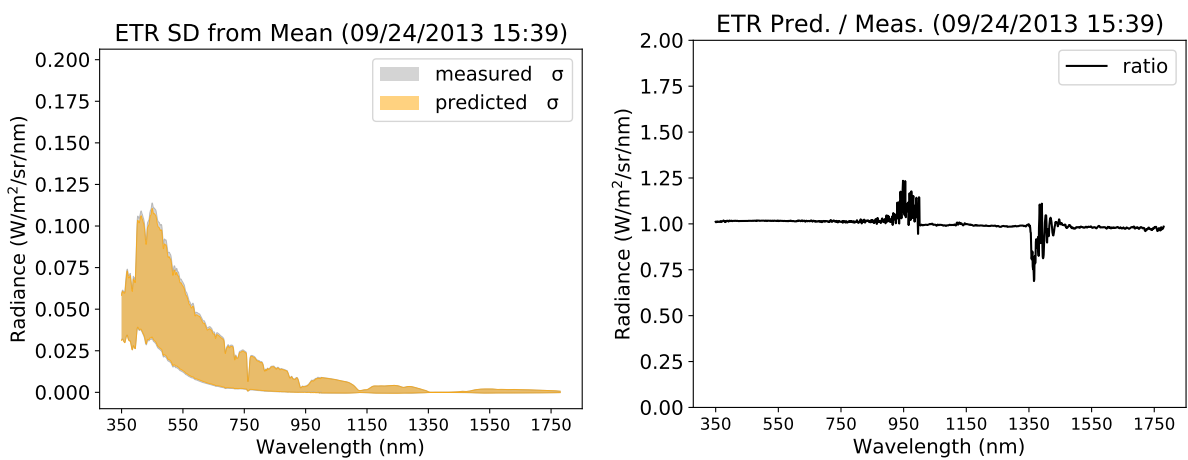
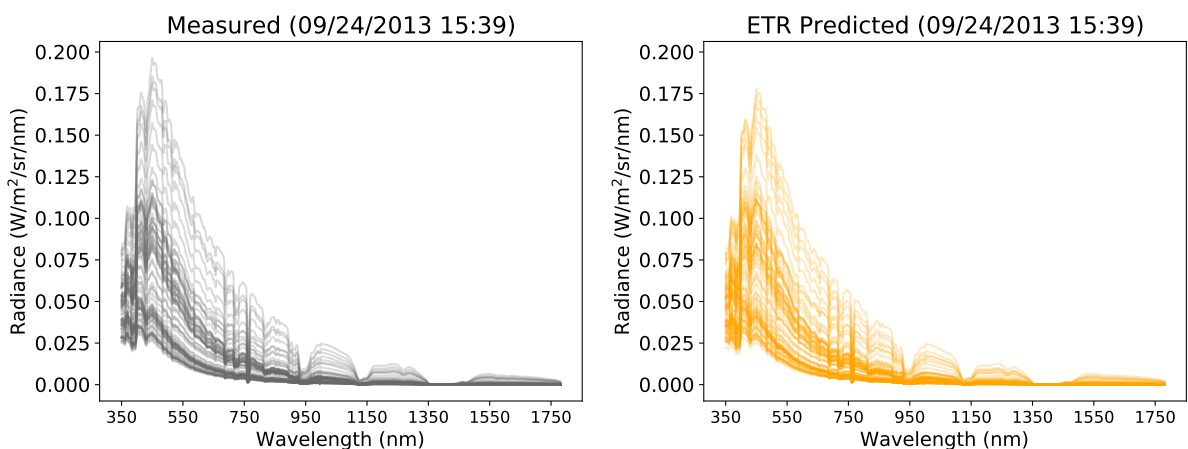
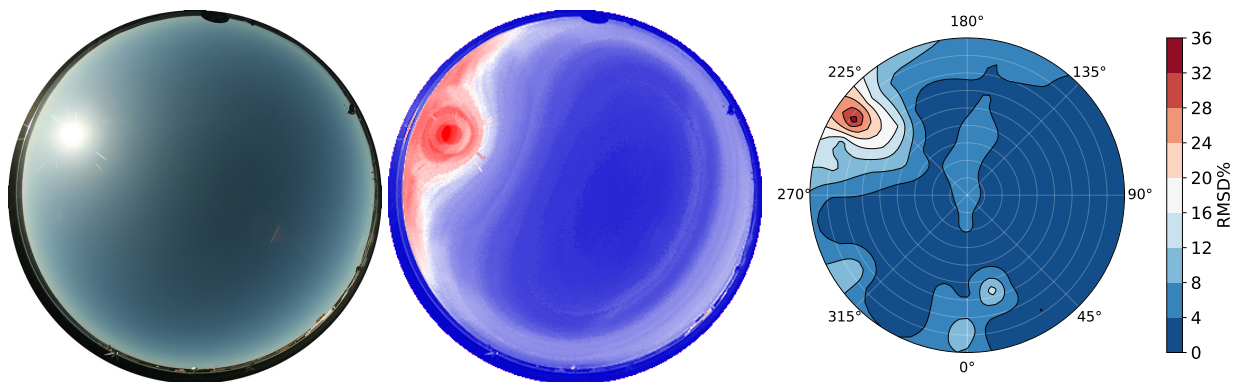
779

780

781 Appendix D - 09/24/13 15:39⁶

782 Whole sky ETR predictions for holdout test sky 09/24/2013 15:39.

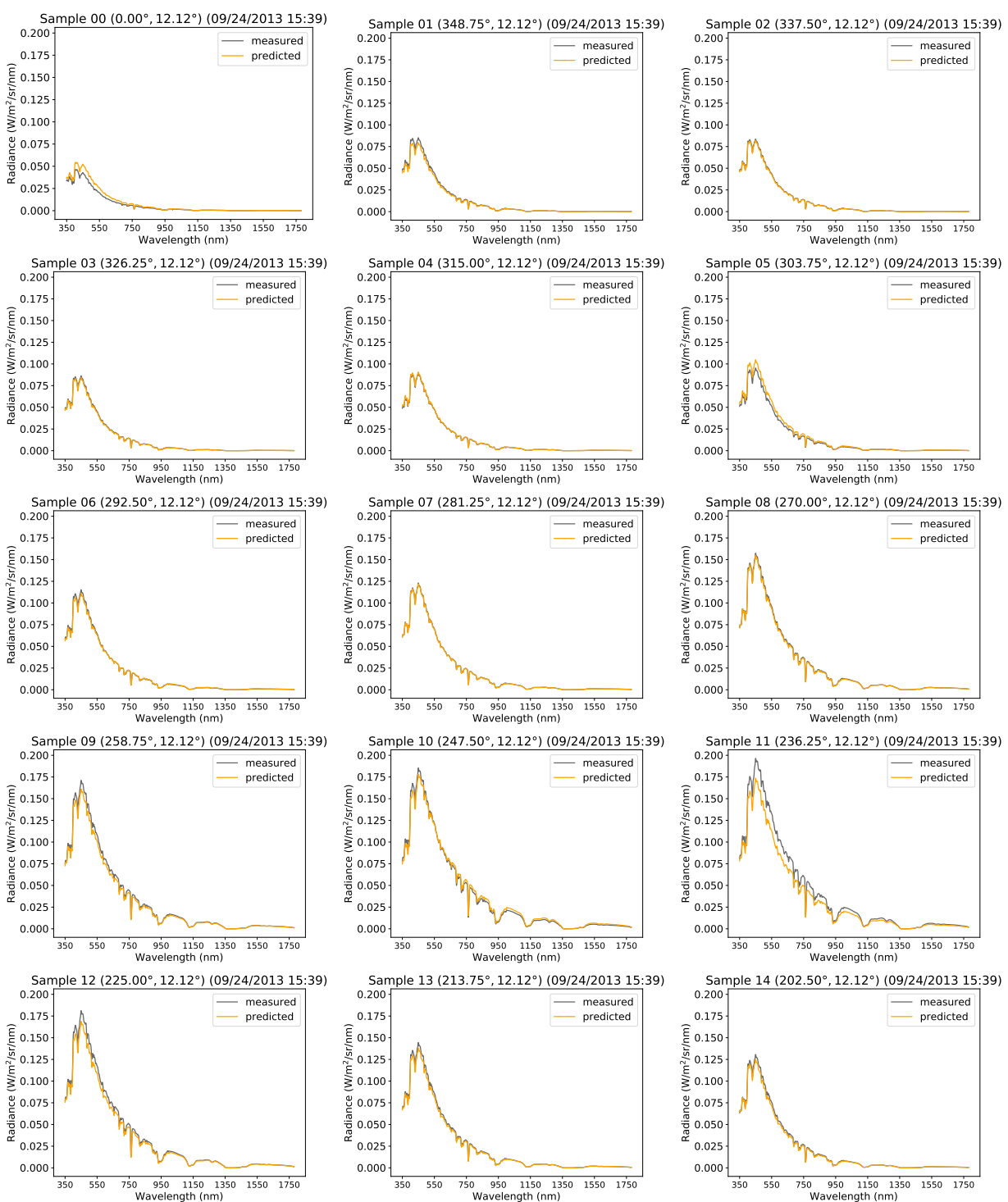
783

⁶Provided for reviewing purposes only.

Real-time spectral radiance estimation of clear skies

787 15 of 81 consecutive ETR spectral radiance predictions for holdout test sky 09/24/2013 15:39.

788



789

790

791

792

793

794